Curvature-induced symmetry breaking determines elastic surface patterns

Norbert Stoop[1], Romain Lagrange[1], Denis Terwagne[2†], Pedro M. Reis[2,3] and Jörn Dunkel[1*]

Symmetry-breaking transitions associated with the buckling and folding of curved multilayered surfaces—which are common to a wide range of systems and processes such as embryogenesis, tissue differentiation and structure formation in heterogeneous thin films or on planetary surfaces—have been characterized experimentally. Yet owing to the nonlinearity of the underlying stretching and bending forces, the transitions cannot be reliably predicted by current theoretical models. Here, we report a generalized Swift–Hohenberg theory that describes wrinkling morphology and pattern selection in curved elastic bilayer materials. By testing the theory against experiments on spherically shaped surfaces, we find quantitative agreement with analytical predictions for the critical curves separating labyrinth, hybrid and hexagonal phases. Furthermore, a comparison to earlier experiments suggests that the theory is universally applicable to macroscopic and microscopic systems. Our approach builds on general differential-geometry principles and can thus be extended to arbitrarily shaped surfaces.

Symmetry breaking and structure formation are intrinsically linked. Symmetry-breaking transitions encompass a diverse range of phenomena, from the emergence of large-scale cosmological structures[1] or the formation of sand dunes[2] to crystallization of solids[3] and the development of form and function in living organisms[4,5]. Theoretical analysis of symmetry breaking typically builds on effective nonlinear field equations that describe complex many-particle systems[6] by a few macroscopic field variables. This approach has proved fruitful in identifying generic aspects of structure formation, as exemplified by the Ginzburg–Landau theory of phase transitions[7] and Turing's description of reaction–diffusion patterns[8,9]. Generally, however, it is challenging to derive nonlinear field theories systematically[10–13] from the underlying microscopic dynamics. Instead, effective field equations are often inferred from abstract symmetry considerations and bifurcation theory[14], resulting in a large number of undetermined parameters that limit the predictive power and complicate comparison with experimental data. Here, we systematically derive and experimentally test an effective field theory that predicts quantitatively the surface-pattern selection in curved bilayer systems consisting of a stiff film on a soft substrate (Figs 1 and 2).

Buckling of thin films plays a prominent role in the morphogenesis of multilayered soft tissues, governing the wrinkling of skin[15], fingerprint formation[16] and the development of brain convolutions[17]. In addition to their biological relevance, wrinkling processes under curvature constraints are attracting considerable interest as promising techniques for nanoscale surface patterning[18], microlens array fabrication[19] and adaptive aerodynamic drag control[20]. Recent experiments and simulations suggest that wrinkling patterns may vary strongly with applied stress[21–25] and substrate curvature[20,26–30]. However, so far, the complexity of the numerically implemented tensor equations has prevented a detailed analytical understanding. Despite substantial progress

in the theoretical description of planar bilayer membranes[31,32], it is unclear how curvature controls pattern selection in non-planar geometries.

The scalar field theory presented below solves this longstanding problem by providing detailed quantitative predictions for curvature- and stress-induced pattern-formation transitions. Starting from Koiter's shell theory[33], we derive a generalized fourth-order Swift–Hohenberg (GSH) equation for the normal displacement field of a film bound to an arbitrarily curved surface (Supplementary Information). In the case of a spherical geometry, our GSH theory reveals that curvature triggers a transition from labyrinth-like to hexagonal wrinkling patterns through a curvature-induced symmetry breaking in the field equation. The theory further predicts a coexistence region separating two 'pure' phases (Fig. 1a–c). Both the theoretically predicted surface patterns and the analytically predicted phase diagram agree quantitatively with data from our macroscale experiments (Figs 1d–f and 3). The GSH model implies that analogous transitions occur when the compressive stress in the film is increased. This prediction is in agreement with recent microscale experiments[28,34] (Fig. 1g–i), suggesting that the theory is universally applicable to both microscopic and macroscopic systems. As our derivation of the GSH model builds on general differential-geometric principles, it can be extended to arbitrarily shaped surfaces, thus providing a generic framework for future studies of curvature-controlled wrinkling in physical, biological and chemical systems.

Theory of thin-film deformation on soft substrates

Our derivation starts from the covariant Koiter shell equations[33], obtained from three-dimensional elasticity theory through an expansion in the film thickness $h \to 0$ (Fig. 2). Koiter's model expresses the elastic energy of a freestanding curved shell in terms of deformations of its central surface (Supplementary Information). Although the Koiter equations have been successfully used in
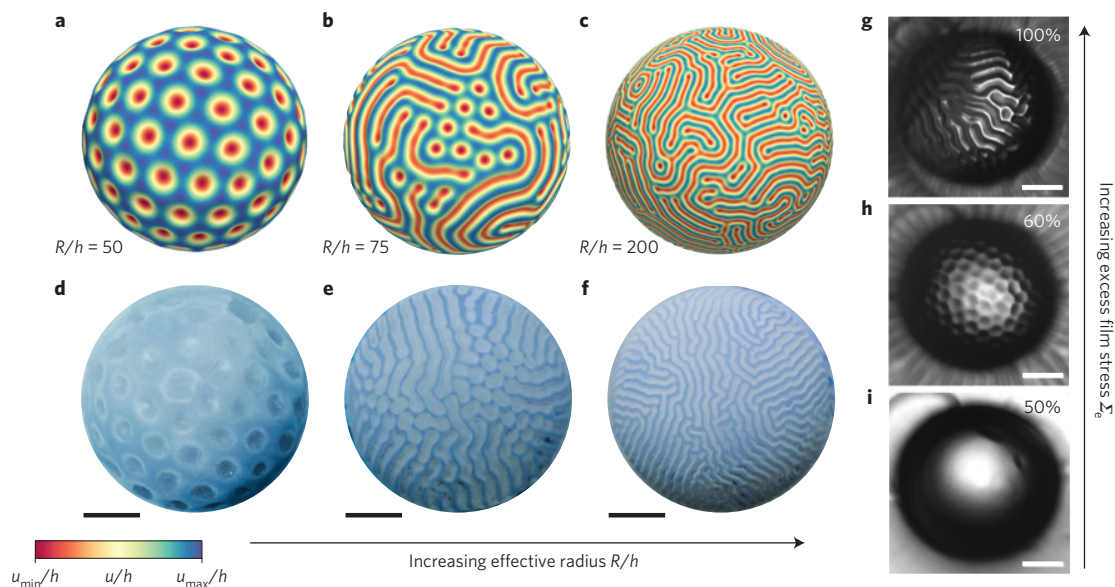
Figure 1 | Macroscopic and microscopic wrinkling morphologies of stiff thin films on spherically curved soft substrates. a–c, Theoretical predictions based on numerical steady-state solutions of equation (1). Colour red (blue) signals inward (outward) wrinkles. Simulation parameters: (**a**) $\gamma_0 = -0.029$, $a = 0.00162$, $c = 0.0025$; (**b**) $\gamma_0 = -0.04$, $a = -1.26 \times 10^{-6}$, $c = 0.002$; (**c**) $\gamma_0 = -0.02$, $a = 1.49 \times 10^{-4}$, $c = 0.0025$ (see Table 1). **d–f**, Experimentally observed patterns confirm the transition from hexagonal (**d**) to labyrinth-like wrinkles (**f**) via a bistable region (**e**) when the radius-to-thickness ratio R/h (see Fig. 2) is increased. Scale bars, 10 mm. Parameters: $E_f = 2{,}100$ kPa, $R = 20$ mm, $\nu = 0.5$ and (**d**) $E_s = 230$ kPa, $h = 0.630$ mm; (**e**) $E_s = 29$ kPa, $h = 0.14$ mm; (**f**) $E_s = 63$ kPa, $h = 0.10$ mm. **g–i**, Oxide layers on microscopic PDMS hemispheres exhibit a similar transition from hexagonal to labyrinth patterns when the excess film stress is increased through changes in the ambient ethanol concentration (indicated in per cent). Scale bars, 250 µm. Micrographs courtesy of D. Breid and A. Crosby[28].
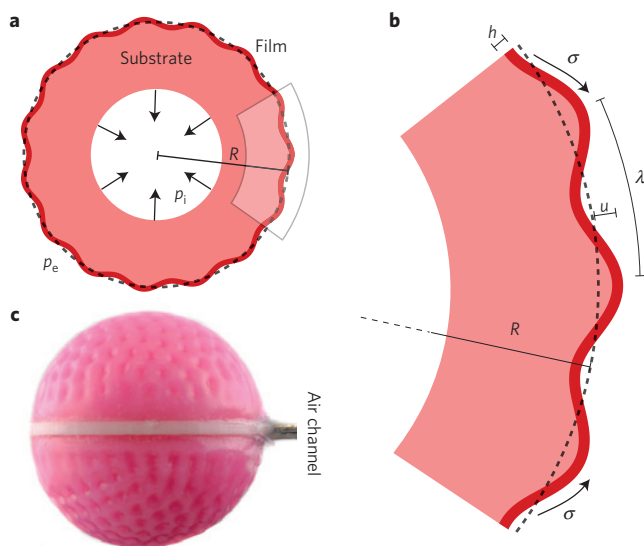

Figure 2 | Notation and experimental system. a, Schematic of a curved thin film adhering to a soft spherical substrate of outer radius R. **b**, The film (thickness h) is driven towards a wrinkling instability by the compressive film stress σ, leading to a wrinkling pattern with wavelength λ and radial displacement u. **c**, The experimental system consists of two merged hemispherical caps. An air channel allows one to tune the film stress σ through the pressure difference $\Delta p = p_e - p_i$.

computational wrinkling studies[26,27], their nonlinear tensorial structure offers limited insight beyond linear stability analysis. We found, however, that substantial analytical simplifications are possible when a stiff film (Young modulus E_f) is adhered to a soft substrate with Young modulus $E_s \ll E_f$.

As relevant to our experiments, which are described in detail below, we consider a spherical geometry with radius $R/h \gg 1$ and

assume that film and substrate have the same Poisson ratio ν. The generalization to non-spherical surfaces is obtained by replacing the metric tensor appropriately (Supplementary Information). Continuity across the film–substrate interface favours deformations that are dominated by the radial displacement u (Fig. 2; from here onwards all lengths are normalized by h). Neglecting secondary lateral displacements, one can systematically expand the strain energy, which contains the original Koiter shell energy density as well as additional substrate coupling and overstress contributions, in terms of the covariant surface derivative ∇u and powers of u (Supplementary Information). Functional variation of the elastic energy with respect to u then yields a nonlinear partial differential equation for the wrinkled equilibrium state of the film. Assuming overdamped relaxation dynamics, one thus obtains the following GSH equation (Supplementary Information)

$$\partial_t u = \gamma_0 \Delta u - \gamma_2 \Delta^2 u - au - bu^2 - cu^3$$
$$+ \Gamma_1 \left[(\nabla u)^2 + 2u\Delta u \right] + \Gamma_2 \left[u(\nabla u)^2 + u^2 \Delta u \right] \quad (1)$$

Here, Δ denotes the Laplace–Beltrami operator, involving the surface metric tensor of the sphere and Christoffel symbols of the second kind, and Δ^2 is the surface biharmonic operator[35]. The (γ_0, γ_2) terms describe stress and bending, the (a, b, c) terms comprise local film–substrate interactions and stretching contributions, and the (Γ_1, Γ_2) terms account for higher-order stretching forces. For $\Gamma_1 = \Gamma_2 = 0$, equation (1) reduces to the standard Swift–Hohenberg equation, as originally derived in the context of Rayleigh–Bénard convection[10,36]. The additional (Γ_1, Γ_2) terms will prove crucial below when matching theory and experiments. The generalization of equation (1) for arbitrary surfaces is given in Supplementary Equation (34).

The detailed derivation (Supplementary Information), combined with systematic asymptotic analysis of the planar limit $R/h \to \infty$, allows us to express the coefficients in equation (1) in terms of the standard material parameters: Poisson ratio of the film ν,
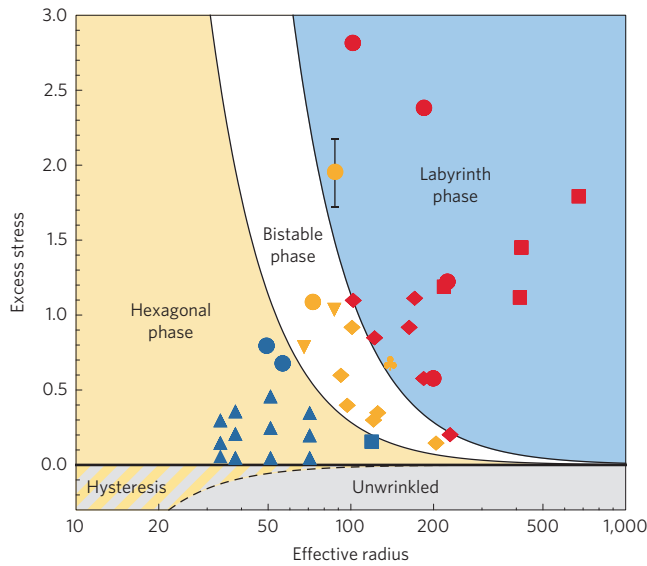
Figure 3 | Phase diagram of wrinkling morphologies. Experimental data points for hexagonal (blue), bistable (yellow) and labyrinth (red) patterns are shown for different values of curvature radius $R/h = \kappa^{-1}$ and excess film stress Σ_e. Symbols indicate the elastic moduli ratio $\eta = 3E_s/E_f$ (square, $\eta = 0.019$; circle, $\eta = 0.036$; clubsuit, $\eta = 0.041$; downtriangle, $\eta = 0.055$; diamond, $\eta = 0.09$; triangle, $\eta = 0.328$). The data suggest that phase boundaries are independent of η in the experimentally tested range. Only the largest vertical error bars are shown (standard deviation of 12 amplitude measurements; see Methods). Horizontal error bars are smaller than the symbol size. Solid lines are theoretically predicted phase boundaries, obtained from equation (3) with parameter $c_1 = 0.0188$ (Table 1).

Table 1 | List of parameters for equation (1) in units $h = 1$, with $\eta = 3E_s/E_f$, $\gamma_2 = 1/12$, $\Sigma_e = (\sigma/\sigma_c) - 1$ and $\kappa = h/R$.

$$\gamma_0 = -\frac{\eta^{2/3}}{6} - \left[\frac{2(1+\nu)}{\eta^{2/3}} - \frac{1}{3}\right]\kappa^2$$

$$a = \frac{\eta^{4/3}}{12} + \frac{6(1+\nu) - \eta^{2/3}}{3}\kappa^2 + \tilde{a}_2 \Sigma_e$$

$$b = 3(1+\nu)\kappa^3$$

$$c = \frac{2(1+\nu)\eta^{2/3}}{3}c_1$$

$$\Gamma_1 = \frac{1+\nu}{2}\kappa$$

$$\Gamma_2 = \frac{1+\nu}{2}\kappa^2$$

$$\tilde{a}_2 = -\frac{\eta^{4/3}(c + 3|\gamma_0|\Gamma_2)}{48\gamma_0^2}$$

The only remaining fitting parameter of the model is c_1.

effective curvature $\kappa = h/R$, Young ratio $\eta = 3E_s/E_f$, and excess stress $\Sigma_e = (\sigma/\sigma_c) - 1$ (Table 1). The theory contains only a single fitting parameter, c_1, related to the cubic stretching force term cu^3. Equation (1) predicts that the unbuckled solution $u = 0$ is stable for negative excess stresses $\Sigma_e < 0$, whereas wrinkling occurs for $\Sigma_e \geq 0$. Linear stability analysis at $\Sigma_e = 0$ and $\kappa = 0$ reproduces the classical[37] pattern-wavelength relation for planar wrinkling, $\lambda/h = 2\pi\eta^{-1/3}$ (Supplementary Information).

Numerical simulation of equation (1) is non-trivial owing to the metric dependence of the biharmonic operator Δ^2 (ref. 35). To compute the stationary wrinkling patterns (Fig. 1a–c) predicted by equation (1), we implemented a C^1-continuous finite-element algorithm specifically designed for covariant fourth-order problems (Methods). A main benefit of equation (1), however, is that it enables analytical prediction of the various pattern-formation regimes.

Pattern selection

Pattern selection in the wrinkling regime $\Sigma_e \geq 0$ is a nonlinear process and, therefore, cannot be inferred from linear stability analysis. Numerical parameter scans of equation (1) yield a variety of qualitatively different stationary states that can be classified as representatives of a hexagonal phase (Fig. 1a), labyrinth phase (Fig. 1c) or intermediate coexistence phase (Fig. 1b). Qualitatively, the transition from hexagons to labyrinths can be understood through a symmetry argument: the (b, Γ_1) terms in equation (1) break the radial reflection invariance of its solutions under the transformation $u \to -u$, as also evident from the corresponding energy functional that is given in Supplementary Equation (37). As b and Γ_1 are controlled by $\kappa = h/R$ (Table 1), we expect a curvature-induced symmetry-breaking transition at some critical value of κ. Furthermore, recalling that the inclusion of similar symmetry-breaking terms causes a transition from labyrinths to hexagonal

patterns in the classical Swift–Hohenberg model[36], it is plausible to expect a hexagonal phase at large curvatures κ and labyrinths at smaller values of κ in our system.

To obtain a quantitative prediction for the phase boundaries, we approximate equation (1) through a standard Swift–Hohenberg equation and make use of established results from nonlinear stability analysis[38]. Assuming plane-wave solutions with amplitude $\mathcal{A}$ and wavevector k, the Γ_1 term exerts an average force $\Gamma_1\langle(\nabla u)^2 + 2u\Delta u\rangle_\lambda = -\Gamma_1\mathcal{A}^2 k^2/2$ per wavelength λ. One may therefore approximate the Γ_1 term by an effective quadratic force $-\Gamma_1 k^2 u^2$, and similarly the Γ_2 term by an effective cubic force $\Gamma_2 k^2 u^3/2$ (Supplementary Information). Inserting for k the most unstable mode, $k_* = \sqrt{|\gamma_0|/(2\gamma_2)}$, equation (1) can be approximated by the standard Swift–Hohenberg equation

$$\partial_t \phi = -2\Delta\phi - \Delta^2\phi - A\phi - B\phi^2 - \phi^3 \quad (2)$$

where $\phi = u/u_*$, $u_* = |\gamma_0|/\sqrt{(c/3) + \Gamma_2|\gamma_0|}$, $A = 3a/\gamma_0^2$, and $B = u_*[(b/3) + 2|\gamma_0|\Gamma_1]/\gamma_0^2$. Nonlinear stability analysis of equation (2) yields the critical phase transition curves as functions of A and B (ref. 38). Note that the coefficients in equation (2) can be directly traced back to geometric and material parameters, whereas in many other pattern formation processes Swift–Hohenberg-type equations have been applied only in a purely phenomenological manner[6]. In terms of the original system parameters, one finds the stability criteria (Supplementary Information)

Hexagonal phase: $-\kappa^2/(20c_1^2) < \Sigma_e < \kappa^2/c_1^2$

Bistable phase: $\kappa^2/c_1^2 < \Sigma_e < 4\kappa^2/c_1^2$ (3)

Labyrinth phase: $4\kappa^2/c_1^2 < \Sigma_e$

where the parameter c_1 sets the strength of the cubic stretching force (Table 1). In the bistable coexistence phase, both hexagon and labyrinth solutions are stable, suggesting a strong dependence on initial conditions in this regime (Fig. 4).

Equation (3) confirms our qualitative symmetry argument and implies, moreover, that the pattern-formation transitions can be controlled not only by curvature, but also through the excess film stress Σ_e, in agreement with recent experimental results[28] (Fig. 1g–i).
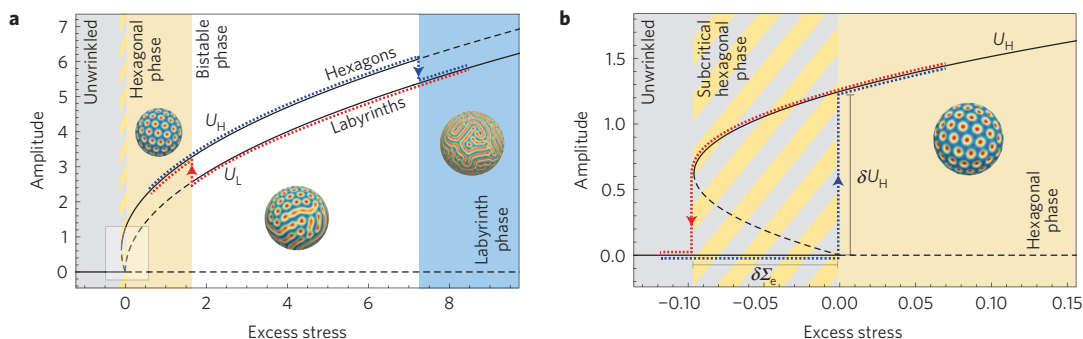
Figure 4 | Bifurcation diagram of wrinkling patterns. Stability analysis of equation (2) predicts two hysteresis cycles, shown here for $R/h = 40$. Solid (dashed) lines correspond to stable (unstable) amplitude solutions; see equation (4) and Supplementary Information. **a**, The hysteresis path across the bistable phase is realized by first decreasing (red) and subsequently increasing (blue) the excess stress Σ_e. **b**, Enlarged view of the second curvature-dependent hysteresis cycle near $\Sigma_e = 0$, corresponding to the highlighted region in **a**. Starting from a stable unwrinkled solution at $\Sigma_e < 0$, the system switches to a hexagonal state at $\Sigma_e = 0$ (blue path). When decreasing the excess stress again to negative values (red), the hexagons remain stable in the subcritical region until a critical value $\Sigma_e = -\delta\Sigma_e$ is reached. The width $\delta\Sigma_e$ and height δU_H of this hysteresis loop depend on curvature $\kappa = h/R$; see equation (4).

Comparison with experiments

We test the theoretical predictions, obtained from equations (1)–(3), by studying the wrinkling of centimetre-sized polydimethylsiloxane (PDMS)-coated elastomer hemispheres (Methods). In our experiments, wrinkling is controlled by the swelling of the film during fabrication and by manual depressurization after fabrication (Fig. 2a,c). The displacement field u, from which the excess film stress Σ_e can be estimated through amplitude measurements[32], is obtained from three-dimensional (3D) surface scans (Methods).

The experimental data confirm quantitatively the theoretically predicted curvature-induced phase transitions from hexagons to labyrinths (Figs 1 and 3). At high values of curvature $\kappa = h/R$, we find the hexagonal phase, characterized by localized spherical depressions that are typically surrounded by 6 neighbours (Fig. 1a,d), although occasional topological defects with 5 or 7 neighbours exist as required by Euler's polyhedral theorem[39]. As predicted by equation (1), experimentally observed hexagons always buckle inwards. For intermediate values of κ, the experiments further confirm coexisting domains of hexagonal and labyrinth-like patterns (Fig. 1b,e). In our simulations of equation (1), we find that the energy of such hybrid patterns remains constant asymptotically, suggesting that they are not transient but correspond to local energy minima. When the curvature is decreased, $\kappa \to 0$, at constant stress Σ_e, the experimental system transitions into the labyrinth phase (Fig. 1c,f), characterized by a network of connected ridges and extended but disconnected valleys (Fig. 1f). Equation (1) shows that this ridge–valley asymmetry is due to the small but non-vanishing symmetry-breaking effect of curvature.

Moreover, in agreement with previous microscale experiments[28] (Fig. 1g–i), equations (1) and (3) imply that the phase transition from hexagons to labyrinths can also be triggered by increasing the excess film stress $\Sigma_e = (\sigma/\sigma_c) - 1$ at constant surface curvature. The morphological phase diagram constructed from our macroscale data confirms this prediction (Fig. 3). In particular, by fixing just a single fitting parameter $c_1 = 0.0188 \pm 0.0002$, the analytical results for the two critical curves in equation (3) are in good quantitative agreement with the experimental data for a wide range of Young modulus ratios $\eta = 3E_s/E_f$ (Fig. 3). Strikingly, we find that the phase boundaries are independent of η over the range $0.019 < \eta < 0.328$ realized in our experiments, suggesting that the parameter c_1 may be a universal numerical constant independent of material properties.

Predictions for future experiments

The good agreement between theory and available experimental data encourages additional predictions that ought to be tested in future experiments. The nonlinear stability analysis of equation (2) suggests that, for sufficiently small overstress Σ_e, the hexagonal phase continues to exist even for weakly curved substrates[32] with $\kappa \ll 1$ (Fig. 3). Simulations of equation (1) for time-varying overstress $\Sigma_e(t)$ confirm that, owing to the presence of symmetry-breaking terms for $\kappa \neq 0$, hexagonal patterns always appear first after crossing the wrinkling threshold $\Sigma_e = 0$ from below. Once the hexagons have been formed, they remain stable throughout the bistable phase when the film stress is slowly increased. A similar reverse effect is observed when the film stress is slowly decreased in simulations that start from the labyrinth phase. In this case, the labyrinths persist throughout the bistable region. Equation (1) makes it possible to understand such memory effects analytically (Fig. 4).

Specifically, the above bifurcation analysis of equations (1)–(3) predicts two hysteresis cycles. The first cycle relates to the onset of wrinkling at $\Sigma_e = 0$ (Fig. 4b), whereas the second encompasses the bistable phase (Fig. 4a). The amplitude $U_H = \max u_H - \min u_H$ of the hexagonal solutions u_H grows according to a square-root law, shifted by the coefficient of the symmetry-breaking term in equation (2) (Supplementary Information),

$$U_H = \frac{3}{5}\left[Bu_* + \sqrt{(Bu_*)^2 + \frac{45\Sigma_e}{4}} \right] \qquad (4)$$

where $Bu_* \simeq 3\kappa/(4c_1)$ to leading order in κ, with B and u_* as defined in equation (2). Equation (4) implies that, for $\kappa > 0$, the hexagonal phase is stable subcritically: on reducing the excess film stress from the hexagonal phase, hexagons remain stable even when the film stress is below the critical wrinkling stress σ_c (Fig. 4b). The width of the subcritical region, $\delta\Sigma_e = \kappa^2/(20c_1^2)$, and the amplitude at onset, $\delta U_H = U_H(\Sigma_e = 0) = 9\kappa/(10c_1)$, scale with κ. The bifurcation at $\Sigma_e = 0$ is transcritical, corresponding to a Lifshitz point[38]. Such bifurcations are typical of Swift–Hohenberg-type models, and have been predicted and observed in optics[40] and nonlinear biological and chemical systems[41]. For values of Σ_e in the subcritical hysteresis region, the hexagonal and the flat state are simultaneously stable in a narrow parameter range, potentially allowing for localized hexagonal patterns as found for the standard Swift–Hohenberg equation[42,43].

The detailed analysis of the second hysteresis cycle (Fig. 4a) shows that the amplitude U_L of the labyrinth solutions follows a square-root law (Supplementary Information). Starting from the labyrinth phase, the system remains in a labyrinth state when the film stress is lowered across the bistable region until one reaches the

instability threshold, located at $\Sigma_e \approx 1.75$ in the depicted example with $R/h = 40$ (red path in Fig. 4a). At that point, the system transitions into a hexagonal state. As Σ_e is increased again, the film maintains the hexagonal configuration until the stress exceeds the upper instability threshold $\Sigma_e \approx 7.5$ (blue path in Fig. 4a).

The direct verification of the two predicted hysteresis cycles poses a substantial experimental challenge, requiring high accuracy in the amplitude measurements and precise reversible tuning mechanisms for the excess film stress Σ_e. For instance, the large stress variations needed to trace out the hysteresis loops with a single sample cannot be realized with the present depressurization set-up[20]. Some preliminary experimental support for the hysteresis predictions comes from a recent study[32] of low-stress films, which pointed out the frequent appearance of hexagonal patterns when the excess stress is slowly varied from negative to positive values (see also Fig. 1g–i). These findings are consistent with the results of the above bifurcation analysis (Fig. 4a). We hope that our detailed theoretical predictions will stimulate further experimental work.

In closing, we showed that a systematically derived effective field theory provides a comprehensive quantitative description of surface-pattern formation in non-planar elastic media (see Supplementary Fig. 2 for additional examples with spatially varying curvature). The observation of similar pattern transitions in systems ranging from a few micrometres[26,28,34] to several centimetres[20,27], combined with the fact that curvature-induced pattern selection can now be understood in terms of a symmetry breaking in the effective field equations, suggests that such processes form common universality classes. The generic differential-geometric framework developed here enables a systematic classification of wrinkling phenomena in complex geometries, by examining the symmetry properties of effective higher-order differential operators built from the surface metric and film–substrate coupling forces. Moreover, equation (1) and its generalization to arbitrary shapes (Supplementary Information) provide a basis for studying weakly time-dependent phenomena such as the nucleation of wrinkling patterns under adiabatic (slow) increase of stress. Thus, in practice, the above analytical approach can help us to predict and control wrinkling processes under natural conditions, promising improved microfabrication techniques and, perhaps, even a better understanding of tissue mechanics and developmental morphogenesis.

Methods

Algorithm. The fourth-order covariant derivatives in the metric-dependent biharmonic operator Δ^2 make it challenging to solve equation (1) numerically. We simulate equation (1) by employing an extension of the finite-element scheme, based on subdivision surface basis functions. Previous studies[44,45] show that this method yields high accuracy and excellent performance for related problems in nonlinear elasticity. The underlying algorithm ensures the C^1-continuity of the basis functions, as required for the numerical integration of fourth-order equations. The method also allows for a direct computation of the various covariant derivatives. As in standard finite-element algorithms, we discretize the spherical surface with a mesh consisting of up to 50,000 triangular elements. A solution coefficient u_i is assigned to each of the $i = 1, \ldots, N$ triangle vertices, such that the system state is interpolated by $u(\mathbf{r}) = \sum_{i=1}^{N} u_i N_i(\mathbf{r})$, where the N_i terms are the finite-element basis functions. For each time step $[t, t + \Delta t]$, we solve the weak form of equation (1) as a sum over individual element-wise contributions. Starting from random initial conditions with $\|u_i\|^2 < 1 - a$, we integrate the dynamics of the system in time using a standard explicit Euler scheme, to obtain the system state $\{u_i\}$ at time $t + \Delta t$. We determine steady-state solutions by continuously monitoring the associated free energy. We consider the system to be in a steady state if its relative change remains below 10^{-5} for more than 10,000 successive time steps.

Experiments. Hemispherical samples were fabricated using rapid digital prototyping techniques that allow flexibility in the choice of geometrical and material parameters[20]. Samples were casted and coated using silicone-based elastomers, such as PDMS (Sylgard 184, Dow Corning), Ecoflex (Smooth-on) and vinylpolysiloxane (VPS, Zhermack), allowing us to examine a wide range of elastic moduli for film (E_f) and substrate (E_s), spanning $9 \leq E_f/E_s \leq 162$. Typical sample parameters are: outer radius $R = 20$ mm, radius of the inner cavity 9 mm,

and film thickness $20\,\mu m \leq h \leq 1{,}000\,\mu m$. The inner cavity of the samples was depressurized to create a state of homogeneous compression and to trigger wrinkling of the stiff surface film. Surface profiles were measured using a NextEngine 3D Laser scanner. The excess film stress Σ_e was estimated from the pattern amplitude $\mathcal{A}$ determined in the 3D surface scans, using the established amplitude versus stress relations $\mathcal{A} = k\sqrt{\Sigma_e}$ from classical wrinkling theory[32], with $k = 1$ for labyrinths and $k = 2/\sqrt{11 + 6\nu - 5\nu^2}$ for hexagonal patterns.

References

1. Bond, J. R., Kofman, L. & Pogosyan, D. How filaments of galaxies are woven into the cosmic web. *Nature* **380,** 603–606 (1996).
2. Parteli, E., Durán, O., Tsoar, H., Schwämmle, V. & Herrmann, H. J. Dune formation under bimodal winds. *Proc. Natl Acad. Sci. USA* **106,** 22085–22089 (2009).
3. Onuki, A. *Phase Transition Dynamics* (Cambridge Univ. Press, 2002).
4. Palmer, A. R. Symmetry breaking and the evolution of development. *Science* **306,** 828–833 (2004).
5. Chirat, R., Moulton, D. E. & Goriely, A. Mechanical basis of morphogenesis and convergent evolution of spiny seashells. *Proc. Natl Acad. Sci. USA* **110,** 6015–6020 (2013).
6. Aranson, I. S. & Tsimring, L. S. Patterns and collective behavior in granular media: Theoretical concepts. *Rev. Mod. Phys.* **78,** 641–692 (2006).
7. Ginzburg, V. L. & Landau, L. D. On the theory of superconductivity. *Zh. Eksp. Teor. Fiz.* **20,** 1064–1082 (1950).
8. Turing, A. M. The chemical basis of morphogenesis. *Phil. Trans. R. Soc. Lond. B* **237,** 37–72 (1952).
9. Ouyang, Q. & Swinney, H. L. Transition from a uniform state to hexagonal and striped Turing patterns. *Nature* **352,** 610–612 (1991).
10. Swift, J. & Hohenberg, P. C. Hydrodynamic fluctuations at the convective instability. *Phys. Rev. A* **15,** 319–328 (1977).
11. Paczuski, M., Kardar, M. & Nelson, D. R. Landau theory of the crumpling transition. *Phys. Rev. Lett.* **60,** 2638–2640 (1988).
12. Delprato, A. M., Samadani, A., Kudrolli, A. & Tsimring, L. S. Swarming ring patterns in bacterial colonies exposed to ultraviolet radiation. *Phys. Rev. Lett.* **87,** 158102 (2001).
13. Brenner, M. P. Chemotactic patterns without chemotaxis. *Proc. Natl Acad. Sci. USA* **107,** 11653–11654 (2010).
14. Wiggins, S. & Golubitsky, M. *Introduction to Applied Nonlinear Dynamical Systems and Chaos* Vol. 2 (Springer-Verlag, 1990).
15. Cerda, E. & Mahadevan, L. Geometry and physics of wrinkling. *Phys. Rev. Lett.* **90,** 074302 (2003).
16. Efimenko, K. *et al.* Nested self-similar wrinkling patterns in skins. *Nature Mater.* **4,** 293–297 (2005).
17. Richman, D. P., Stewart, R. M., Hutchinson, J. W. & Caviness, V. S. Mechanical model of brain convolutional development. *Science* **189,** 18–21 (1975).
18. Bowden, N., Brittain, S., Evans, A. G., Hutchinson, J. W. & Whitesides, G. M. Spontaneous formation of ordered structures in thin films of metals supported on an elastomeric polymer. *Nature* **393,** 146–149 (1998).
19. Chan, E. P. & Crosby, A. J. Fabricating microlens arrays by surface wrinkling. *Adv. Mater.* **18,** 3238–3242 (2006).
20. Terwagne, D., Brojan, M. & Reis, P. M. Smart morphable surfaces for aerodynamic drag control. *Adv. Mater.* **26,** 6608–6611 (2014).
21. Jiang, H. *et al.* Finite deformation mechanics in buckled thin films on compliant supports. *Proc. Natl Acad. Sci. USA* **104,** 15607–15612 (2007).
22. Pocivavsek, L. *et al.* Stress and fold localization in thin elastic membranes. *Science* **320,** 912–916 (2008).
23. Brau, F. *et al.* Multiple-length-scale elastic instability mimics parametric resonance of nonlinear oscillators. *Nature Phys.* **7,** 56–60 (2011).
24. Xu, F., Potier-Ferry, M., Belouettar, S. & Cong, Y. 3d finite element modeling for instabilities in thin films on soft substrates. *Int. J. Solids Struct.* **51,** 3619–3632 (2014).
25. Brau, F., Damman, P., Diamant, H. & Witten, T. A. Wrinkle to fold transition: Influence of the substrate response. *Soft Matter* **9,** 8177–8186 (2013).
26. Cao, G., Chen, X., Li, C., Ji, A. & Cao, Z. Self-assembled triangular and labyrinth buckling patterns of thin films on spherical substrates. *Phys. Rev. Lett.* **100,** 036102 (2008).
27. Li, B., Jia, F., Cao, Y.-P., Feng, X.-Q. & Gao, H. Surface wrinkling patterns on a core-shell soft sphere. *Phys. Rev. Lett.* **106,** 234301 (2011).
28. Breid, D. & Crosby, A. J. Curvature-controlled wrinkle morphologies. *Soft Matter* **9,** 3624–3630 (2013).
29. Schroll, R. D. *et al.* Capillary deformations of bendable films. *Phys. Rev. Lett.* **111,** 014301 (2013).

341

30. King, H., Schroll, R. D., Davidovitch, B. & Menon, N. Elastic sheet on a liquid drop reveals wrinkling and crumpling as distinct symmetry-breaking instabilities. *Proc. Natl Acad. Sci. USA* **109,** 9716–9720 (2012).
31. Audoly, B. & Boudaoud, A. Buckling of a thin film bound to a compliant substrate, part i: Formulation, linear stability of cylindrical patterns, secondary bifurcations. *J. Mech. Phys. Solids* **56,** 2401–2421 (2008).
32. Cai, S., Breid, D., Crosby, A. J., Suo, Z. & Hutchinson, J. W. Periodic patterns and energy states of buckled films on compliant substrates. *J. Mech. Phys. Solids* **59,** 1094–1114 (2011).
33. Ciarlet, P. G. *Mathematical Elasticity* Vol. 3 (North Holland, 2000).
34. Yin, J., Han, X., Cao, Y. & Lu, C. Surface wrinkling on polydimethylsiloxane microspheres via wet surface chemical oxidation. *Sci. Rep.* **4,** 5710 (2014).
35. Jost, J. *Riemannian Geometry and Geometric Analysis* (Springer, 2008).
36. Cross, M. C. & Hohenberg, P. C. Pattern formation outside of equilibrium. *Rev. Mod. Phys.* **65,** 851–1112 (1993).
37. Allen, H. G. *Analysis and Design of Structural Sandwich Panels* (Pergamon, 1969).
38. Golovin, A. A. & Nepomnyashchy, A. A. *Self-Assembly, Pattern Formation and Growth Phenomena in Nano-Systems* (Springer, 2006).
39. Coxeter, H. S. M. *Regular Polytopes* (Courier Dover Publications, 1973).
40. Clerc, M. G., Petrossian, A. & Residori, S. Bouncing localized structures in a liquid-crystal light-valve experiment. *Phys. Rev. E* **71,** 015205(R) (2005).
41. Kozyreff, G. & Tlidi, M. Nonvariational real Swift–Hohenberg equation for biological, chemical, and optical systems. *Chaos* **17,** 037103 (2007).
42. Lloyd, D. J. B., Sandstede, B., Avitabile, D. & Champneys, A. R. Localized hexagon patterns of the planar Swift–Hohenberg equation. *SIAM J. Appl. Dyn. Syst.* **7,** 1049–1100 (2008).
43. Burke, J. & Knobloch, E. Localized states in the generalized Swift–Hohenberg equation. *Phys. Rev. E* **73,** 056211 (2006).
44. Cirak, F., Ortiz, M. & Schröder, P. Subdivision surfaces: A new paradigm for thin-shell finite-element analysis. *Int. J. Numer. Methods Eng.* **47,** 2039–2072 (2000).
45. Stoop, N., Wittel, F. K., Amar, M. B., Müller, M. M. & Herrmann, H. J. Self-contact and instabilities in the anisotropic growth of elastic membranes. *Phys. Rev. Lett.* **105,** 068101 (2010).

Author contributions

N.S., R.L. and J.D. developed the theory. N.S. and R.L. performed analytical calculations. N.S. implemented and performed the numerical simulations. D.T. and P.M.R. developed the experiments. N.S., R.L. and D.T. analysed data. All authors discussed the results and contributed to writing the paper.

Additional information

Supplementary information is available in the online version of the paper. Reprints and permissions information is available online at www.nature.com/reprints. Correspondence and requests for materials should be addressed to J.D.

Competing financial interests

The authors declare no competing financial interests.

Curvature-induced symmetry breaking determines elastic surface patterns

Norbert Stoop[1], Romain Lagrange[1], Denis Terwagne[2*], Pedro M. Reis[2,3], and Jörn Dunkel[1]

[1]*Department of Mathematics, Massachussetts Institute of Technology,*
77 Massachusetts Avenue, Cambridge, MA 02139-4307, USA

[2]*Department of Civil & Environmental Engineering, Massachussetts Institute of Technology,*
77 Massachusetts Avenue, Cambridge, MA 02139-4307, USA

[3]*Department of Mechanical Engineering, Massachussetts Institute of Technology,*
77 Massachusetts Avenue, Cambridge, MA 02139-1713, USA

(Dated: December 14, 2014)

We derive an effective theory for the wrinkling of thin hard films bound to arbitrarily curved soft substrates. Starting from the nonlinear Koiter shell equations, we show that the elastic equations can be reduced to a generalized Swift-Hohenberg theory, yielding Eq. (1) in the Main Text for the special case of a spherical surface geometry. Using nonlinear analysis of this effective fourth-order equation, we derive predictions for hexagonal and labyrinth-like wrinkling patterns in dependence on the film stress and the substrate curvature. To illustrate the effects of spatially varying substrate curvature on wrinkling, we present additional numerical results for a toroidal geometry.

DEFINITIONS

Let $\boldsymbol{S} = \boldsymbol{\Theta}(\theta_1, \theta_2)$ be a two-dimensional surface in $\mathbb{R}^3$, parameterized by $y = (\theta_1, \theta_2) \in \omega \subset \mathbb{R}^2$. Throughout, Greek indices $\alpha, \beta, \ldots$ take values in $\{1, 2\}$, whereas Latin indices $i, j, \ldots$ run from 1 to 3. The induced metric $a_{\alpha\beta}$ (first fundamental form) on the surface $\boldsymbol{S} = \boldsymbol{\Theta}(\theta_1, \theta_2)$ is given by

$$a_{\alpha\beta} = \boldsymbol{a}_\alpha \cdot \boldsymbol{a}_\beta = a_{\beta\alpha}, \tag{1}$$

where

$$\boldsymbol{a}_\alpha = \boldsymbol{\Theta}_{,\alpha} \equiv \partial_\alpha \boldsymbol{\Theta} \equiv \frac{\partial \boldsymbol{\Theta}}{\partial \theta_\alpha} \tag{2}$$

are the tangent vectors, and $\cdot$ denotes the Euclidean inner product on $\mathbb{R}^3$. The unit-length normal vector $\boldsymbol{n}$ is defined by

$$\boldsymbol{n} \equiv \boldsymbol{a}^3 = \frac{\boldsymbol{a}_1 \times \boldsymbol{a}_2}{|\boldsymbol{a}_1 \times \boldsymbol{a}_2|} \tag{3}$$

and characterized by the properties

$$\boldsymbol{n} \cdot \boldsymbol{n} = 1, \qquad \boldsymbol{n} \cdot \boldsymbol{a}_\alpha = 0, \qquad \boldsymbol{n}_{,\alpha} \cdot \boldsymbol{n} = 0$$
$$\boldsymbol{n}_{,\alpha} \cdot \boldsymbol{a}_\beta = -\boldsymbol{a}_{\alpha,\beta} \cdot \boldsymbol{n}, \qquad \boldsymbol{n} \cdot \boldsymbol{n}_{,\alpha\beta} = -\boldsymbol{n}_{,\alpha} \cdot \boldsymbol{n}_{,\beta}$$

The surface element is

$$d\omega = \sqrt{|\det(a_{\alpha\beta})|}\, dy \tag{4}$$

We also introduce the second and third fundamental forms $b_{\alpha\beta}$, $c_{\alpha\beta}$ with components given by

$$b_{\alpha\beta} = \boldsymbol{n} \cdot \boldsymbol{a}_{\alpha,\beta} \tag{5a}$$
$$c_{\alpha\beta} = \boldsymbol{n}_{,\alpha} \cdot \boldsymbol{n}_{,\beta} \tag{5b}$$

The second fundamental form, $b_{\alpha\beta}$, is often also referred to as the curvature tensor. The Christoffel symbols are

$$\Gamma^\sigma_{\alpha\beta} = \frac{1}{2} a^{\sigma\gamma} \left(a_{\gamma\alpha,\beta} + a_{\gamma\beta,\alpha} - a_{\alpha\beta,\delta} \right) \tag{6}$$

where $a^{\alpha\beta}$ are the components of the contravariant metric tensor, defined by $a^{\alpha\gamma} a_{\beta\gamma} = \delta^\alpha_\beta$. Introducing $\boldsymbol{a}^\alpha = a^{\alpha\beta} \boldsymbol{a}_\beta$, the following identities will be useful later:

$$\boldsymbol{n}_\alpha = -b_{\alpha\beta} \boldsymbol{a}^\beta = -b^\sigma_\alpha \boldsymbol{a}_\sigma \tag{7a}$$
$$b^\gamma_\alpha b_{\beta\gamma} = \boldsymbol{n}_{,\alpha} \cdot \boldsymbol{n}_{,\beta} = c_{\alpha\beta} \tag{7b}$$

The covariant derivative of a scalar function ψ is

$$\nabla_\alpha \psi = \psi_{,\alpha} \tag{8}$$

The gradient of ψ on the surface $\boldsymbol{S}$ has components

$$\nabla^\alpha \psi = a^{\alpha\beta} \nabla_\alpha \psi \tag{9}$$

The action of the Laplace-Beltrami operator $\triangle$ on scalar functions is defined as

$$\triangle \psi = \nabla_\alpha \nabla^\alpha \psi = a^{\gamma\delta} \psi_{,\gamma\delta} - a^{\gamma\delta} \Gamma^\lambda_{\gamma\delta} \psi_{,\lambda} \tag{10}$$

For a vector field V^α or for a $(0,1)$−tensor field V_α, the covariant derivative involves the Christoffel symbols,

$$\nabla_\alpha V^\beta = V^\beta_{,\alpha} + \Gamma^\alpha_{\beta\gamma} V^\gamma \tag{11a}$$
$$\nabla_\alpha V_\beta = V_{\beta,\alpha} - \Gamma^\gamma_{\alpha\beta} V_\gamma \tag{11b}$$

All gradients ∇ and Laplacians $\triangle$ below refer to these surface-specific differential operators.

---

*Current address: Faculté des Sciences, Université Libre de Bruxelles (ULB), Bruxelles 1050, Belgium

ENERGY FUNCTIONAL

We extend the classical Koiter shell (KS) energy functional to account for film-substrate coupling and excess stresses.

Koiter shell equations

The KS equations describe the equilibrium of a thin shell (precurved plate) when the thickness h of the shell is small compared to its curvature in undeformed and deformed configurations. The KS equations follow rigorously by means of Γ-convergence from the full 3D elasticity problem in the limit $h \to 0$ [1].

In the absence of forces and boundary conditions, we assume that the shell adopts a stress-free equilibrium configuration which we call the reference configuration, parametrized by the surface map $\boldsymbol{\Theta}$, with fundamental forms $a_{\alpha\beta}, b_{\alpha\beta}$ etc. as specified above. Under the influence of forces and boundary conditions, the shell adopts a new, deformed configuration characterized by a displacement field $\boldsymbol{\Psi}$ defined with respect to the curved reference state $\boldsymbol{\Theta}$,

$$\boldsymbol{\Psi} = \Psi_1 \boldsymbol{a}^1 + \Psi_2 \boldsymbol{a}^2 + \Psi_3 \boldsymbol{a}^3 \equiv \Psi_i \boldsymbol{a}^i \tag{12}$$

For any point $y \in \omega$, its displaced position is given by $\boldsymbol{\Theta}(y) + \boldsymbol{\Psi}(y)$, and the respective surface geometry will be denoted as $a_{\alpha\beta}(\boldsymbol{\Psi}), b_{\alpha\beta}(\boldsymbol{\Psi})$ etc.

The KS energy of the shell is given by [1]

$$\mathcal{E}_{\mathrm{KS}}(\boldsymbol{\Psi}) = \mathcal{E}_b(\boldsymbol{\Psi}) + \mathcal{E}_s(\boldsymbol{\Psi}) + \mathcal{E}_f(\boldsymbol{\Psi}) \tag{13a}$$

with bending energy

$$\mathcal{E}_b = \frac{E_f}{2(1-\nu^2)} \int_\omega d\omega \, \frac{h^3}{24} C^{\alpha\beta\gamma\delta} R_{\gamma\delta}(\boldsymbol{\Psi}) R_{\alpha\beta}(\boldsymbol{\Psi}) \tag{13b}$$

stretching energy

$$\mathcal{E}_s = \frac{E_f}{2(1-\nu^2)} \int_\omega d\omega \, \frac{h}{2} C^{\alpha\beta\gamma\delta} G_{\gamma\delta}(\boldsymbol{\Psi}) G_{\alpha\beta}(\boldsymbol{\Psi}) \tag{13c}$$

and energy contributions

$$\mathcal{E}_f = -\int_\omega d\omega \, p^i \Psi_i \tag{13d}$$

due to external forces p^i (pressure, body loads, etc.). In Eqs. (13), E_f denotes the Young modulus of the film, ν its Poisson ratio and $C^{\alpha\beta\gamma\delta}$ the constitutive tensor. We focus on the case of a Kirchhoff-St. Venant material, corresponding to an extension of Hook's law to large deformations, described by

$$C^{\alpha\beta\gamma\delta} = (1-\nu)(a^{\alpha\delta}a^{\beta\gamma} + a^{\alpha\gamma}a^{\beta\delta}) + 2\nu a^{\alpha\beta}a^{\gamma\delta} \tag{14}$$

The nonlinear membrane bending and stretching strains $R_{\alpha\beta}$ and $G_{\alpha\beta}$ are given by [1]

$$R_{\alpha\beta} = b_{\alpha\beta}(\boldsymbol{\Psi}) - b_{\alpha\beta} \tag{15a}$$

$$G_{\alpha\beta} = \frac{1}{2}[a_{\alpha\beta}(\boldsymbol{\Psi}) - a_{\alpha\beta}] \tag{15b}$$

The bending energy scales with h^3 and will be small compared to the stretching contributions. We will therefore linearize $R_{\alpha\beta}(\boldsymbol{\Psi})$ in the bending energy, but keep higher-order terms in the stretching strains $G_{\alpha\beta}$.

Normal component of bending strains. The linearized bending strains read [1]

$$R_{\alpha\beta} \simeq (\boldsymbol{\Psi}_{,\alpha\beta} - \Gamma^\sigma_{\alpha\beta}\boldsymbol{\Psi}_{,\sigma}) \cdot \boldsymbol{n} \tag{16}$$

With this approximation, the normal displacement component Ψ_3 decouples from the in-plane components. Since the dominant bending contribution comes from the normal displacement Ψ_3, we may neglect the in-plane components

$$R_{\alpha\beta} \simeq \rho_{\alpha\beta}(\Psi_3) \equiv \Psi_{3,\alpha\beta} - \Gamma^\sigma_{\alpha\beta}\Psi_{3,\sigma} - \Psi_3 c_{\alpha\beta}$$
$$= \nabla_\alpha \nabla_\beta \Psi_3 - \Psi_3 c_{\alpha\beta} \tag{17}$$

Normal component of stretching strains. For the stretching strains, one has [1]

$$G_{\alpha\beta} = \frac{1}{2}(\nabla_\beta \Psi_\alpha + \nabla_\alpha \Psi_\beta + \boldsymbol{\Psi}_{,\alpha} \cdot \boldsymbol{\Psi}_{,\beta}) - b_{\alpha\beta}\Psi_3$$
$$= \frac{1}{2}(\Psi_{\alpha,\beta} + \Psi_{\beta,\alpha} + \boldsymbol{\Psi}_{,\alpha} \cdot \boldsymbol{\Psi}_{,\beta}) - \Gamma^\sigma_{\alpha\beta}\Psi_\sigma - b_{\alpha\beta}\Psi_3 \tag{18}$$

The displacement derivative can be split into an in-plane and normal part,

$$\boldsymbol{\Psi}_{,\alpha} = (\Psi_{\gamma,\alpha} - \Gamma^\sigma_{\alpha\gamma}\Psi_\sigma - b_{\alpha\gamma}\Psi_3)\boldsymbol{a}^\gamma + (\Psi_{3,\alpha} + b^\gamma_\alpha \Psi_\gamma)\boldsymbol{a}^3$$

Due to the orthogonality of $\boldsymbol{a}^\alpha$ and $\boldsymbol{n} \equiv \boldsymbol{a}^3$, the nonlinear term in the stretching strains becomes

$$\boldsymbol{\Psi}_{,\alpha} \cdot \boldsymbol{\Psi}_{,\beta} = t^\delta_\alpha t_{\beta\delta} + s_\alpha s_\beta \tag{19a}$$

where

$$t_{\alpha\beta} = \Psi_{\beta,\alpha} - \Gamma^\sigma_{\alpha\beta}\Psi_\sigma - b_{\alpha\beta}\Psi_3 \tag{19b}$$

$$s_\alpha = \Psi_{3,\alpha} + b^\sigma_\alpha \Psi_\sigma \tag{19c}$$

Expanding Eqs. (19) for small in-plane displacements, $|\Psi_\alpha| \ll |\Psi_3|$, one finds to leading order

$$\boldsymbol{\Psi}_{,\alpha} \cdot \boldsymbol{\Psi}_{,\beta} \simeq \Psi_{3,\alpha}\Psi_{3,\beta} + b^\delta_\alpha b_{\beta\delta}(\Psi_3)^2$$

Using Eq. (7) and (18), we obtain

$$G_{\alpha\beta} \simeq \gamma_{\alpha\beta}(\Psi_3) \equiv \frac{1}{2}[\Psi_{3,\alpha}\Psi_{3,\beta} + c_{\alpha\beta}(\Psi_3)^2] - b_{\alpha\beta}\Psi_3 \tag{20}$$

We note that the obtained bending and stretching strains are symmetric,

$$\rho_{\alpha\beta} = \rho_{\beta\alpha}, \qquad \gamma_{\alpha\beta} = \gamma_{\beta\alpha} \tag{21}$$

Additional remarks. In our and previous [2] experiments, the film stress is imposed in two ways: (i) depressurization of the shell-substrate system and (ii) swelling of the film. Before the onset of the buckling transition, either technique creates a pre-stress in the film. The associated prestrain can be decomposed into an in-plane part $\bar{\gamma}_{\alpha\beta}$ and a bending part $\bar{\rho}_{\alpha\beta}$, with $\bar{\gamma}_{\alpha\beta} \gg \bar{\rho}_{\alpha\beta}$. Adopting the same approximations as above (Eqs. 17, 20), the prestrains remain symmetric. Restricting ourselves furthermore to equi-biaxial pre-stress without shear, $\bar{\gamma}_{\alpha\beta}$ is proportional to the metric tensor $a_{\alpha\beta}$, and we write this as

$$\bar{\gamma}_{\alpha\beta} = \bar{\gamma}\, a_{\alpha\beta} \qquad (22)$$

where from now on $\bar{\gamma}$ denotes the constant of proportionality.

If the film stress due to depressurization or swelling becomes too large, the film will buckle, with an inhomogeneous deformation u around the pre-stressed state. The strains of a buckled configuration can then be expressed as

$$\gamma_{\alpha\beta}(u_0 + u) = \bar{\gamma}_{\alpha\beta} + \frac{1}{2}\left(u_{,\alpha}u_{,\beta} - 2b_{\alpha\beta}u + c_{\alpha\beta}u^2\right) \tag{23a}$$

$$\rho_{\alpha\beta}(u_0 + u) = \bar{\rho}_{\alpha\beta} + \nabla_\alpha\nabla_\beta u - c_{\alpha\beta}u \tag{23b}$$

To contract the strains with the constitutive tensor, we use the fact that the bending and stretching strains, Eqs. (23), are symmetric. For any symmetric $(0,2)$-tensor $\tau_{\alpha\beta}$, the contraction $\mathcal{C}(\tau)$ of $C^{\alpha\beta\gamma\delta}$ with $\tau_{\alpha\beta}$ can be written as

$$\begin{aligned}
\mathcal{C}(\tau) &= C^{\alpha\beta\gamma\delta}\tau_{\alpha\beta}\tau_{\gamma\delta} \\
&= 2\left[(1-\nu)\tau^{\alpha\beta}\tau_{\alpha\beta} + \nu(\tau_\gamma^\gamma)^2\right] \\
&= 2\left(\tau_M + \tau_G\right) \tag{24}
\end{aligned}$$

with

$$\begin{aligned}
\tau_M &= (\tau_\gamma^\gamma)^2 \\
\tau_G &= (1-\nu)\left[\tau^{\alpha\beta}\tau_{\alpha\beta} - (\tau_\gamma^\gamma)^2\right] \tag{25}
\end{aligned}$$

For later use, it is convenient to introduce the identities

$$\mathcal{H} = \frac{1}{2}b_\gamma^\gamma \tag{26a}$$

$$\mathcal{K} = \det(\{a_{\alpha\beta}\})/\det(\{b_{\alpha\beta}\}) \tag{26b}$$

$$\mathcal{R} \equiv b^{\alpha\beta}b_{\alpha\beta} = c_\gamma^\gamma = 4\mathcal{H}^2 - 2\mathcal{K} \tag{26c}$$

$$\mathcal{S} \equiv b^{\alpha\beta}c_{\alpha\beta} = 2\mathcal{H}(4\mathcal{H}^2 - 3\mathcal{K}) \tag{26d}$$

$$\mathcal{T} \equiv c^{\alpha\beta}c_{\alpha\beta} = 16\mathcal{H}^2(\mathcal{H}^2 - \mathcal{K}) + 2\mathcal{K}^2 \tag{26e}$$

$\mathcal{H}$ is the mean curvature and $\mathcal{K}$ the Gaussian curvature. Most of these expressions follow directly from the contracted Gauss-Codazzi-Mainardi equations [3].

Relevant energy contributions

Bending energy density. Using the definition of the Laplace-Beltrami operator, Eq. (10), and Eq. (24) with $\tau_{\alpha\beta} = \rho_{\alpha\beta}$, the mean-curvature contribution ρ_M can be written as

$$\begin{aligned}
\rho_M = \left(\rho_\gamma^\gamma\right)^2 = (\triangle u)^2 - 2\mathcal{R}u\triangle u + \mathcal{R}^2 u^2 + \\
2(\bar{\rho}_\gamma^\gamma\triangle u - \mathcal{R}\bar{\rho}_\gamma^\gamma u) + (\bar{\rho}_\gamma^\gamma)^2 \tag{27}
\end{aligned}$$

The ρ_G-term in Eq. (24) accounts for the energy cost due to a change of Gaussian curvature. This term is negligible if the typical wrinkling wavelengths are small compared to the local radii of curvature of the underlying surface. More precisely, in this case, one finds that Eqs. (15a,17) reduce to $\rho_\alpha^\beta \simeq b_\alpha^\beta(u)$ in leading order, where $b_\alpha^\beta(u)$ is the curvature tensor of the deformed configuration. Accordingly, Eq. (25) then yields $\rho_G = (1-\nu)\mathcal{K}(u)$. Since the Gaussian curvature $\mathcal{K}(u)$ of the deformed configuration integrates to a topological invariant for a closed surface (or when the geodesic curvature of the boundary curve is fixed), the ρ_G-term can be neglected in the variational formulation, just as in the classical Helfrich model [4]. Under these assumptions, the resulting bending energy takes the form

$$\begin{aligned}
\mathcal{E}_b = \frac{E_f}{2(1-\nu^2)}\int_\omega d\omega\, \frac{h^3}{12}\Big[(\triangle u)^2 + 2\mathcal{R}(\nabla u)^2 + \\
(\mathcal{R}^2 - \triangle\mathcal{R})u^2 + \\
2\left(\triangle\bar{\rho}_\gamma^\gamma - \mathcal{R}\bar{\rho}_\gamma^\gamma\right)u + (\bar{\rho}_\gamma^\gamma)^2\Big] \tag{28}
\end{aligned}$$

where from now on the product symbol $\cdot$ as in $(\nabla u)^2 = (\nabla u)\cdot(\nabla u)$ denotes the scalar product with respect to the surface metric. To obtain Eq. (28), we used the generalized Stokes theorem[1] to rewrite the second and fourth term on the rhs. of Eq. (27).

Stretching energy density. For the stretching energy

$$\mathcal{E}_s = \frac{E_f}{2(1-\nu^2)}\int_\omega d\omega\, \frac{h}{2}\mathcal{C}(\gamma) \tag{29}$$

we find by using Eq. (24) with $\tau_{\alpha\beta} = \gamma_{\alpha\beta}$, and combining with Eqs. (22), (23) and (26),

$$\begin{aligned}
\mathcal{C}(\gamma) = 2(1+\nu)\bar{\gamma}(\nabla u)^2 + 2(1+\nu)(\nabla u)^4 - \\
2\left[(1-\nu)b^{\alpha\beta}\nabla_\alpha u\nabla_\beta u + 2\nu\mathcal{H}(\nabla u)^2\right]u + \\
\left[(1-\nu)c^{\alpha\beta}\nabla_\alpha u\nabla_\beta u + \nu\mathcal{R}(\nabla u)^2\right]u^2 + \\
2\left[(1-\nu+\bar{\gamma}+\nu\bar{\gamma})\mathcal{R} + 4\nu\mathcal{H}^2\right]u^2 - \\
2\left[(1-\nu)\mathcal{S} + 2\nu\mathcal{H}\mathcal{R}\right]u^3 + \\
\frac{1}{2}\left[(1-\nu)\mathcal{T} + \nu\mathcal{R}^2\right]u^4 + \mathcal{O}(1) + \mathcal{O}(u) \tag{30}
\end{aligned}$$

————

[1] Note that $-\int d\omega\, \mathcal{R}u\triangle u = \int d\omega\, u(\nabla\mathcal{R})\cdot(\nabla u) + \int d\omega\, \mathcal{R}(\nabla u)^2$. Furthermore, repeated application of the Stokes theorem gives $\int d\omega\, u(\nabla\mathcal{R})\cdot(\nabla u) = \frac{1}{2}\int d\omega\, \triangle\mathcal{R}u^2$.

where we did not explicitly write down the terms linear and constant in u, as they will not be relevant for the later analysis (see detailed remarks in *Total energy density* below).

Substrate coupling energy. In our experiments, the thin film is coupled to a curved soft substrate. To simplify further analysis, we assume from now on that the substrate has the same Poisson ratio ν as the film, as is the case in our experiments. We model the substrate coupling as a nonlinear spring by adding a substrate energy $\mathcal{E}_{sub}$ to the KS energy from Eq. (13a), where

$$\mathcal{E}_{sub} = \frac{E_s}{2} \int_\omega d\omega \left(Au + \frac{\tilde{a}}{h} u^2 + \frac{\tilde{c}}{h^3} u^4 \right) \quad (31)$$

with E_s denoting the Young modulus of the substrate. The constant film thickness h could have been absorbed into the coefficients $\tilde{a}$ and $\tilde{c}$, but simplifies subsequent formulas. Note that $\mathcal{E}_{sub}$ contains a term linear in u because we are considering the state of the film-substrate system around a flat but displaced equilibrium solution u_0. This linear term gives rise to a corresponding constant normal force that is needed to balance the internal normal forces of the film.

Energy due to excess film stress. Finally, we still have to account for the excess film stress

$$\Sigma_e \equiv \frac{\sigma}{\sigma_c} - 1 \quad (32a)$$

where σ is the film stress and σ_c the critical stress needed for wrinkling. In our model, the energy due to excess film stress is included by adding a term

$$\mathcal{E}_\sigma = \frac{E_f}{2(1-\nu^2)} \int_\omega d\omega \, \frac{\tilde{a}_2}{h} \Sigma_e u^2 \quad (32b)$$

to the KS energy from Eq. (13a). The energy contribution $\mathcal{E}_\sigma$ is crucial for capturing the system behavior beyond the wrinkling instability. We discuss below how the dimensionless parameter $\tilde{a}_2$ is related to the elastic properties of the substrate. The u^2-dependence of $\mathcal{E}_\sigma$ is a classical result from elastic wrinkling theory [5], ensuring that the amplitude-stress relationship in the effective model agrees with classical wrinkling theory, as is shown in detail further below.

Total energy density. Adding the contributions due to substrate coupling, external forces and excess stress to the KS energy (13a), we obtain the total elastic energy

$$\mathcal{E} = \frac{E_f}{1-\nu^2} \bar{\mathcal{E}} \quad (33a)$$

where to leading order

$$\bar{\mathcal{E}} = \int_\omega d\omega \left[\frac{\gamma_0}{2} (\nabla u)^2 + \frac{\gamma_2}{2} (\triangle u)^2 + \frac{a}{2} u^2 + \frac{b}{3} u^3 + \frac{c}{4} u^4 - \right.$$
$$\frac{h}{2} \left[(1-\nu) b^{\alpha\beta} \nabla_\alpha u \nabla_\beta u + 2\nu \mathcal{H} (\nabla u)^2 \right] u +$$
$$\left. \frac{h}{4} \left[(1-\nu) c^{\alpha\beta} \nabla_\alpha u \nabla_\beta u + \nu \mathcal{R} (\nabla u)^2 \right] u^2 \right] \quad (33b)$$

with coefficients

$$\gamma_0 = h\bar{\gamma}(1+\nu) + \frac{h^3 \mathcal{R}}{6}$$

$$\gamma_2 = \frac{h^3}{12}$$

$$a = h \left[(1 - \nu + \bar{\gamma} + \nu\bar{\gamma}) \mathcal{R} + 4\nu \mathcal{H}^2 \right] + \frac{h^3(\mathcal{R}^2 - \triangle\mathcal{R})}{12} +$$
$$\frac{E_s(1-\nu^2)}{E_f} \frac{\tilde{a}}{h} + \frac{\tilde{a}_2}{h} \Sigma_e$$

$$b = -\frac{3h}{2} \left[(1-\nu)\mathcal{S} + 2\nu\mathcal{H}\mathcal{R} \right]$$

$$c = \frac{h}{2} \left[(1-\nu)\mathcal{T} + \nu\mathcal{R}^2 \right] + 2\frac{E_s(1-\nu^2)}{E_f} \tilde{c} \quad (33c)$$

Note that for compressive stresses $\bar{\gamma} < 0$. Thus, for sufficiently large film pre-stress, $\gamma_0 < 0$. To obtain the effective energy functional (33), the following additional simplifications and assumptions were adopted:

- **Constant terms.** We neglected all constant terms in the energy, as they will not contribute to the equations of motion, obtained by variation of the energy with respect to u.

- **Terms linear in u.** We note that the term linear in u gives rise to a inhomogeneous, constant term in the equation of motion. However, $u = 0$ always is an equilibrium solution by construction. More precisely, $u = 0$ means that the film is radially displaced by u_0, which is a fundamental solution of the problem. Therefore, the inhomogeneous term in the equation of motion has to vanish, implying that the coefficient of the energy term linear in u must be zero. This condition can be interpreted as follows: For $u = 0$ to be an equilibrium solution, the sum of all normal forces acting on the film must vanish.

- **Quartic terms.** The quartic terms in u and ∇u ensure that the effective theory remains stable above the wrinkling threshold, as these terms limit the growth of the most unstable modes. To keep the theory as simple as possible, we only include the dominant u^4-contribution and neglect terms $\propto (\nabla u)^4$.

Taking the variation of $\bar{\mathcal{E}}$ with respect to u, we obtain

$$-\frac{\delta\bar{\mathcal{E}}}{\delta u} = \gamma_0 \triangle u - \gamma_2 \triangle^2 u - au - bu^2 - cu^3 +$$
$$\frac{h}{2} \left\{ (\nu - 1) \left[b^{\alpha\beta} \nabla_\alpha u \nabla_\beta u + 2u \nabla_\beta \left(b^{\alpha\beta} \nabla_\alpha u \right) \right] +$$
$$2\nu \left[\mathcal{H} (\nabla u)^2 - 2\nabla \cdot (\mathcal{H} u \nabla u) \right] \right\} +$$
$$\frac{h}{2} \left[(1-\nu) u \nabla_\beta \left(u c^{\alpha\beta} \nabla_\alpha u \right) - \nu \mathcal{R} u (\nabla u)^2 +$$
$$\nu \nabla \cdot (\mathcal{R} u^2 \nabla u) \right] \quad (34)$$

where $\nabla\cdot$ denotes the surface divergence. We note that, for a flat Euclidean metric, the first line of Eq. (34) coincides with the Swift-Hohenberg (SH) equation, as originally derived in the context of Rayleigh-Bénard convection [6, 7]. The b-term and the first term $\propto h$ (second and third line) break the symmetry $u \to -u$, which is known to lead to a transition from labyrinth-like patterns to hexagons for SH-like equations. As both terms depend on the curvature tensor $b_{\alpha\beta}$, we can infer that regions of high curvature will show different wrinkling patterns than regions of low curvature.

We next apply Eq. (34) to derive quantitative predictions for wrinkling patterns transitions on spherical geometries, which are then compared with our experiments (Main Text). Subsequently, we still present numerical solutions for a toroidal geometry, as an example of a surface with locally varying curvature.

APPLICATION TO SPHERICAL GEOMETRIES

Using spherical coordinates $(\theta_1, \theta_2) \in [0, 2\pi] \times [0, \pi]$, a spherical surface of radius R is described by the metric tensor

$$(a_{\alpha\beta}) = \begin{pmatrix} (R\sin\theta_2)^2 & 0 \\ 0 & R^2 \end{pmatrix} \qquad (35)$$

In this case, we have $\mathcal{H} = -1/R$, $\mathcal{K} = 1/R^2$. Thus

$$\mathcal{R} = 2/R^2, \qquad \mathcal{S} = -2/R^3, \qquad \mathcal{T} = 2/R^4 \qquad (36)$$

Total energy density. Noting that the sphere has constant mean and Gaussian curvature $\mathcal{H}$ and $\mathcal{K}$, Eq. (36) allows to simplify the total energy density (33) considerably,

$$\bar{\mathcal{E}} = \int_\omega d\omega \left[\frac{\gamma_0}{2}(\nabla u)^2 + \frac{\gamma_2}{2}(\triangle u)^2 + \frac{a}{2}u^2 + \frac{b}{3}u^3 + \frac{c}{4}u^4 + \right.$$
$$\left. \Gamma_1 (\nabla u)^2 u + \frac{\Gamma_2}{2}(\nabla u)^2 u^2 \right] \qquad (37)$$

with coefficients

$$\gamma_0 = h\bar{\gamma}(1+\nu) + \frac{h^3}{3R^2}$$

$$\gamma_2 = \frac{h^3}{12}$$

$$a = \frac{2h(1+\bar{\gamma})(1+\nu)}{R^2} + \frac{h^3}{3R^4} + \frac{E_s(1-\nu^2)}{E_f}\frac{\tilde{a}}{h} + \frac{\tilde{a}_2}{h}\Sigma_e$$

$$b = \frac{3h(1+\nu)}{R^3}$$

$$c = \frac{h(1+\nu)}{R^4} + 2\frac{E_s(1-\nu^2)}{E_f}\tilde{c}$$

$$\Gamma_1 = \frac{h(1+\nu)}{2R}$$

$$\Gamma_2 = \frac{h(1+\nu)}{2R^2} \qquad (38)$$

Equations of motions

To identify the equilibrium configurations, we assume that the film exhibits an overdamped relaxation dynamics. Then, the equations of motion follow by functional variation of the elastic energy (37) with respect to the displacement field u,

$$\frac{\rho}{\tau_0}\partial_t u = -\frac{\delta\mathcal{E}}{\delta u} \qquad (39)$$

where ρ is the constant surface mass density of the film and τ_0 the damping-time scale. The relaxation dynamics (39) can be written in the equivalent form

$$\mu\partial_t u = -\frac{\delta\bar{\mathcal{E}}}{\delta u} \qquad (40a)$$

where the coefficient

$$\mu = \frac{\rho(1-\nu^2)}{\tau_0 E_f} \qquad (40b)$$

is the inverse relaxation speed. Calculating the functional derivative $\delta\bar{\mathcal{E}}/\delta u$ gives

$$\mu\partial_t u = \gamma_0\triangle u - \gamma_2\triangle^2 u - au - bu^2 - cu^3 + \qquad (41)$$
$$\Gamma_1\left[(\nabla u)^2 + 2u\triangle u\right] + \Gamma_2\left[u(\nabla u)^2 + u^2\triangle u\right]$$

Since we are only interested in the steady-state solutions, the exact value of μ is not relevant for our analysis. It is convenient to rewrite Eq. (41) in dimensionless form by measuring length in units of the film thickness h and time in units of $\tau_h = \mu h$. Introducing the dimensionless curvature parameter

$$\kappa = h/R \qquad (42)$$

Eq. (41) reduces to

$$\partial_t u = \gamma_0\triangle u - \gamma_2\triangle^2 u - au - bu^2 - cu^3 + \qquad (43)$$
$$\Gamma_1\left[(\nabla u)^2 + 2u\triangle u\right] + \Gamma_2\left[u(\nabla u)^2 + u^2\triangle u\right]$$

with rescaled dimensionless parameters

$$\gamma_0 = \bar{\gamma}(1+\nu) + \frac{\kappa^2}{3} < 0$$

$$\gamma_2 = \frac{1}{12}$$

$$a = 2(1+\bar{\gamma})(1+\nu)\kappa^2 + \frac{\kappa^4}{3} + \frac{E_s(1-\nu^2)}{E_f}\tilde{a} + \tilde{a}_2\Sigma_e$$

$$b = 3(1+\nu)\kappa^3$$

$$c = (1+\nu)\kappa^4 + 2\frac{E_s(1-\nu^2)}{E_f}\tilde{c}$$

$$\Gamma_1 = \frac{(1+\nu)\kappa}{2}$$

$$\Gamma_2 = \frac{(1+\nu)\kappa^2}{2} \qquad (44)$$

Note that the covariant derivatives ∇ and $\triangle$ in Eq. (43) are now also defined with respect to the rescaled dimensionless sphere of radius $\kappa^{-1} = R/h$. In Eq. (44), we kept the term $\sim \kappa^4$ in the coefficient a. Although this higher order term is negligible, its inclusion will lead to simpler expressions when matching our model with experiments (see section *Curvature-dependence of the critical strain $\bar{\gamma}$* below). Given the dimensionless parameters in Eq. (44), the corresponding values in physical units are recovered through the transformations

$$
\begin{aligned}
u &\to hu, & R &\to h/\kappa, & t &\to \mu ht \\
\gamma_0 &\to h\gamma_0, & \gamma_2 &\to h^3\gamma_2 \\
a &\to a/h, & b &\to b/h^2, & c &\to c/h^3 \\
\Gamma_1 &\to \Gamma_1, & \Gamma_2 &\to \Gamma_2/h
\end{aligned}
\tag{45}
$$

As evident from Eq. (44), the model is specified through dimensionless parameters

$$
(\kappa, \bar{\gamma}, E_s/E_f, \nu, \tilde{a}, \tilde{a}_2, \tilde{c})
\tag{46}
$$

Parameter determination

The parameters (h, R, ν, E_s, E_f) can be directly measured for our experimental system. To determine the remaining parameters $(\bar{\gamma}, \tilde{a}, \tilde{a}_2, \tilde{c})$, we proceed as follows:

1. Linear stability analysis will enable us to relate γ_0 at the onset of wrinkling with the wavelength λ, which yields a relation between the critical buckling strain $\bar{\gamma}$ and the ratio E_s/E_f.

2. The value of the substrate parameter $\tilde{a}$ can be estimated from known results for the critical bulking stress in planar elasticity theory [8]. Below, we will extend the classical derivation to the weakly curved case to confirm that our model predictions agree with recent results by Cai *et al.* [9]

3. By means of nonlinear stability analysis and comparison with analytical results for the standard Swift-Hohenberg equation, we will express the parameter $\tilde{a}_2$ in terms of c, leaving $\tilde{c}$ as the only remaining fit parameter. We estimate $\tilde{c}$ by comparing our numerical simulations with the experimentally measured surface morphologies.

Critical stress $\bar{\gamma}$ and $\tilde{a}$

We estimate $\bar{\gamma}$ by comparing our effective theory with known results for the full elastic equations in the planar limit case $R \to \infty$. Letting $\kappa \to 0$ and linearizing Eq. (43) for a small perturbation εe^{ikx} of the unbuckled

homogeneous solution, one finds the dominant unstable wave-mode

$$
|k| = \sqrt{\frac{|\gamma_0|}{2\gamma_2}} = \sqrt{6|\gamma_0|}
\tag{47a}
$$

which selects the characteristic wavelength

$$
\lambda_c = \frac{2\pi}{|k|} = \frac{2\pi}{\sqrt{6|\gamma_0|}}
\tag{47b}
$$

Equating λ_c with the known wrinkling wavelength λ_{el} of a planar elastic film-substrate system, which in units $h = 1$ is given by [8]

$$
\lambda_{el} = 2\pi \left(\frac{E_f}{3E_s}\right)^{1/3}
\tag{48}
$$

we obtain

$$
\gamma_0 = -\frac{1}{6}\left(\frac{3E_s}{E_f}\right)^{2/3}
\tag{49}
$$

The sign indicates a compressive strain, which in our terminology is negative. From Eq. (44) with $\kappa \to 0$, we find the planar estimate

$$
\bar{\gamma} \simeq -\frac{1}{6(1+\nu)}\left(\frac{3E_s}{E_f}\right)^{2/3} \equiv \bar{\gamma}_p
\tag{50}
$$

A correction due to curvature will be discussed below.

Critical stress. The strain $\bar{\gamma}_p$ can be associated with the critical stress σ_c at the wrinkling threshold. As expressed by Eq. (22), our system is in a state of equibiaxial strains $\bar{\gamma}$ implying that, in a locally orthogonal coordinate frame, the in-plane elasticity tensor reduces to $\epsilon_{11} = \epsilon_{22} = \epsilon$, $\epsilon_{12} = \epsilon_{21} = 0$. The usual stress-strain relationship of a Hookean material then reads [10]

$$
\sigma_{11} = \sigma_{22} = \frac{E}{1-\nu^2}(\epsilon_{11} + \nu\epsilon_{22}) = \frac{E}{1-\nu}\epsilon \equiv \sigma
$$
$$
\sigma_{12} = \sigma_{21} = 0
$$

Assuming a standard linear relation between stress and strain, we expect

$$
\sigma_c = k_\sigma \frac{E_f}{1-\nu}\bar{\gamma}_p
\tag{51}
$$

with some constant prefactor k_σ. Inserting Eq. (50), we obtain

$$
\sigma_c = -\frac{k_\sigma}{6}\frac{E_f}{1-\nu^2}\left(\frac{3E_s}{E_f}\right)^{2/3}
\tag{52}
$$

which for $k_\sigma = 3/2$ agrees with the known critical stress of elastic wrinkling analysis [8]

$$
\sigma_{c_{el}} = -\frac{E_f}{4(1-\nu^2)}\left(\frac{3E_s}{E_f}\right)^{2/3}
\tag{53}
$$

Estimation of $\tilde{a}$ near the critical value σ_c. In the planar limit $\kappa \to 0$, Eq. (43) exhibits a bifurcation from a uniform state to nontrivial pattern formation only if $a < a_c$, where

$$a_c = \frac{\gamma_0^2}{4\gamma_2} = \frac{1}{12}\left(\frac{3E_s}{E_f}\right)^{4/3} \qquad (54)$$

At the wrinkling onset, corresponding to $a = a_c$, the film stress σ equals the critical stress σ_c so that $\Sigma_e = 0$. For the planar case, Eq. (54) thus determines the substrate parameter $\tilde{a}$ as

$$\tilde{a} = \frac{1}{4(1-\nu^2)}\left(\frac{3E_s}{E_f}\right)^{1/3} \qquad (55)$$

Curvature-dependence of the critical strain $\bar{\gamma}$

Recent simulations of the full coupled elasticity equations [11] and experiments with polymer colloids [12] report wave-length reduction of pattern on curved substrates compared with the planar case. It is therefore interesting to study how the critical strain $\bar{\gamma} < 0$ depends on the curvature parameter $\kappa = h/R$ in our model.

Similar to the planar case, cf. Eq. (54), the wrinkling bifurcation occurs when

$$\frac{\gamma_0^2(\kappa)}{4\gamma_2\, a_c(\kappa)} = 1. \qquad (56)$$

Recalling that $\Sigma_e = 0$ at the transition point and using the the above result for $\tilde{a}$, we can solve Eq. (56) for the critical strain $\bar{\gamma}$. Using Eq. (44) we then obtain for γ_0

$$\gamma_0 = \frac{\kappa^2}{3} - \frac{1}{6}\sqrt{\left(\frac{3E_s}{E_f}\right)^{4/3} + 24(1+\nu)\kappa^2} \qquad (57)$$

which reduces to Eq. (49) in the planar case ($\kappa = 0$). For $\bar{\gamma}$, we find to $\mathcal{O}(\kappa^4)$

$$\frac{\bar{\gamma}}{\bar{\gamma}_p} = 1 + 12\kappa^2(1+\nu)\left(\frac{E_f}{3E_s}\right)^{4/3} \qquad (58)$$

where $\bar{\gamma}_p$ is the critical buckling strain for the planar case, given in Eq. (50). This asymptotic scaling behavior in κ is similar to the results of Cai *et al.* [9], although the numerical prefactors and the dependence on the Poisson ratio ν differ.

According to Eq. (57), the absolute value $|\gamma_0|$ increases with curvature with a leading order correction $\sim \kappa^2$. Equation (47b) then implies that the wavelength λ_c decreases with increasing curvature, in qualitative agreement with experimental and numerical findings [11, 12]. It is interesting to note that the wavelength reduction in our model is due to the nonlinear, curvature-dependent stretching terms of the underlying KS energy, unlike the

γ_0	$=$	$-\dfrac{\eta^{2/3}}{6} - \left[\dfrac{2(1+\nu)}{\eta^{2/3}} - \dfrac{1}{3}\right]\kappa^2$
a	$=$	$\dfrac{\eta^{4/3}}{12} + \dfrac{6(1+\nu) - \eta^{2/3}}{3}\kappa^2 + \tilde{a}_2\Sigma_e$
b	$=$	$3(1+\nu)\kappa^3$
c	$=$	$\dfrac{2(1+\nu)\eta^{2/3}}{3}c_1$
Γ_1	$=$	$\dfrac{1+\nu}{2}\kappa$
Γ_2	$=$	$\dfrac{1+\nu}{2}\kappa^2$
$\tilde{a}_2$	$=$	$-\dfrac{\eta^{4/3}(c + 3|\gamma_0|\Gamma_2)}{48\gamma_0^2}$

TABLE I: List of parameters for Eqs. (43) and (64) as obtained by systematic asymptotic matching to classical elastic wrinkling theory, with $\eta = 3E_s/E_f$, $\gamma_2 = 1/12$, $\Sigma_e = (\sigma/\sigma_c) - 1$, and $\kappa = h/R$ where h is the film thickness and R the radius (see Fig. 2 of Main Text). We substituted $\tilde{a}$ and $\tilde{c}$ by Eqs. (55) and (77). Focusing on the leading order contribution, we only kept terms up to $\mathcal{O}(\kappa^3)$, cf. Eq. (57). The only remaining fitting parameter of the model is c_1.

model of Yin *et al.* [13], where a wavelength reduction was obtained by assuming a curvature-dependent substrate model. Unfortunately, for the range of parameters realized in our experiments the curvature-induced wavelength reduction is below the detection threshold. We therefore did not include any curvature-dependent substrate response in our model.

Nonlinear behavior above onset

Having determined estimates for the parameters $(\bar{\gamma}, \tilde{a})$ by analyzing the onset of wrinkling, the two remaining unknown parameters are $(\tilde{a}_2, \tilde{c})$. Aiming to further reduce the number of free parameters, we now turn to the regime beyond the wrinkling threshold, where patterns are selected by nonlinear effects. To this end, we first reduce the generalized Swift-Hohenberg equation (43) to a standard Swift-Hohenberg (SH) equation by approximating mixed $\Gamma_{1,2}$-terms in Eq. (43) that contain both u and ∇u through effective expressions that only contain u. Assuming a typical relation between pattern amplitude and excess film stress $\Sigma_e = (\sigma/\sigma_c) - 1$, we can then exploit existing results for the stability of patterns in the SH equation to predict the morphological phase diagram of the wrinkling patterns in our experimental system.

Swift-Hohenberg approximation. To approximate Eq. (43) by a standard SH equation, we recall that γ_0 and γ_2 select the dominant (most unstable) wave number vector $k_c = \pm\sqrt{6|\gamma_0|}$, see Eq. (47a). Considering the

limit $\kappa \to 0$ and a plane-wave solution of the form

$$u = \mathcal{A}\cos(k_c x) \qquad (59)$$

the Γ_1-term in Eq. (43) exerts an average force per wavelength $\lambda = 2\pi/|k_c|$ of

$$\left\langle \Gamma_1\left[(\nabla u)^2 + 2u\triangle u\right]\right\rangle_\lambda = -\frac{1}{2}\Gamma_1\mathcal{A}^2 k_c^2 \qquad (60)$$

where

$$\langle f(x)\rangle_\lambda \equiv \frac{1}{\lambda}\int_0^\lambda dx\, f(x) \qquad (61)$$

Comparing Eq. (60) with the average force exerted by a quadratic force $f = au^2$ for the wave solution (59),

$$\langle au^2\rangle_\lambda = \frac{a\mathcal{A}^2}{2} \qquad (62)$$

we can approximate the Γ_1-term by an 'equivalent' average force term of the form

$$\Gamma_1\left[(\nabla u)^2 + 2u\triangle u\right] \approx -\Gamma_1 k_c^2 u^2 \qquad (63\mathrm{a})$$

Similarly, the average force due to the Γ_2-term can be approximated by a cubic force. Since the Γ_2-term is antisymmetric in u, the corresponding mean force is obtained by averaging over the interval $[\lambda/4, 3\lambda/4]$, yielding

$$\Gamma_2\left[u(\nabla u)^2 + u^2\triangle u\right] \approx -\frac{1}{2}\Gamma_2 k_c^2 u^3 \qquad (63\mathrm{b})$$

With these approximations, Eq. (43) reduces to the SH equation

$$\partial_t u = \gamma_0\triangle u - \gamma_2\triangle^2 u -$$
$$au - \left(b + \Gamma_1 k_c^2\right)u^2 - \left(c + \frac{\Gamma_2 k_c^2}{2}\right)u^3 \qquad (64)$$

To facilitate direct comparison with results in the literature [14], it is convenient to rewrite Eq. (64) in the rescaled *normal form*

$$\partial_T\phi = -2\triangle_X\phi - \triangle_X^2\phi - A\phi - B\phi^2 - \phi^3 \qquad (65)$$

where

$$T = \frac{4\gamma_2 t}{\gamma_0^2} = \frac{t}{3\gamma_0^2}$$
$$\triangle_X = \frac{\triangle}{k_c^2} = \frac{\triangle}{6|\gamma_0|}$$
$$\phi = \frac{u}{u_*} \qquad (66)$$
$$u_* = \sqrt{\frac{\gamma_0^2}{4\gamma_2(c + \Gamma_2 k_c^2/2)}} = \sqrt{\frac{\gamma_0^2}{(c/3) + \Gamma_2|\gamma_0|}}$$
$$A = \frac{a}{a_c} = \frac{4a\gamma_2}{\gamma_0^2} = \frac{3a}{\gamma_0^2}$$
$$B = \frac{2\left(b + \Gamma_1 k_c^2\right)}{\sqrt{(\gamma_0^2/\gamma_2)(c + \Gamma_2 k_c^2/2)}} = u_*\frac{(b/3) + 2|\gamma_0|\Gamma_1}{\gamma_0^2}$$

with a_c given by Eq. (54).

Excess film stress. Our model accounts for the excess film stress $\Sigma_e = (\sigma/\sigma_c) - 1$ through the contribution $\tilde{a}_2\Sigma_e$ that appears in the coefficient a of the linear force, see Eq. (44). This specific functional relationship between a and Σ_e follows from the requirement that, in the planar limit $\kappa \to 0$, our model must produce the same amplitude-stress relation as classical wrinkling theory [5]. More precisely, classical planar wrinkling theory predicts that the amplitude $\mathcal{A}_{el}$ of the wrinkling solution $u = \mathcal{A}_{el}\cos(kx)$, measured in units of the film thickness h, is equal to square of the excess film stress [9],

$$\mathcal{A}_{el} = \sqrt{\Sigma_e}. \qquad (67)$$

This must be equal to the amplitude $\mathcal{A}$ of the solution $u = \mathcal{A}\cos(k_c x)$ of the standard SH equation (64), which is given by [14]

$$\mathcal{A} = \frac{2}{\sqrt{3}}u_*\sqrt{1 - A} \qquad (68)$$

Equating the amplitudes yields

$$A = \frac{a}{a_c} = 1 - \frac{3\Sigma_e}{4u_*^2} \qquad (69)$$

Finally, considering the definition of a in Eq. (44) in the planar case $\kappa = 0$ and inserting a_c from Eq. (54), we find

$$\tilde{a}_2 = -\frac{3\gamma_2}{4u_*^2}\left(\frac{3E_s}{E_f}\right)^{4/3} \qquad (70)$$

We have thus determined all parameters of the effective theory with the exception of $\tilde{c}$, which enters through both c in Eq. (44) and u_* in (70), see Eq. (66). As shown in the next section, $\tilde{c}$ can be estimated by matching our model predictions with the experiments. Table I summarizes the results for our model parameters, retaining curvature terms up to $\mathcal{O}(\kappa^3)$, and is also reproduced in Table 1 of the Main Text.

Remark. In the above derivation, we have matched the amplitude-stress relationship using the plane-wave wrinkling solution. Alternatively, one can match the amplitude-stress relationship of wrinkling patterns using the hexagonal solution of the SH equation. The general procedure is identical to the one above. The hexagonal solution u_H of the standard SH equation is given by [14]

$$u_\mathrm{H} = \mathcal{A}\left[\cos(k_c x) + 2\cos\left(\frac{k_c x}{2}\right)\cos\left(\frac{\sqrt{3}k_c y}{2}\right)\right] \qquad (71)$$

with

$$\mathcal{A} = \frac{2}{15}\left[Bu_* + \sqrt{(Bu_*)^2 + 15u_*^2(1 - A)}\right] \qquad (72)$$

B vanishes in the planar case, where $\kappa = 0$. Classical planar wrinkling theory predicts the same solution, Eq. (71), with amplitude [9]

$$\mathcal{A}_{el} = \frac{2}{\sqrt{11 + 6\nu - 5\nu^2}}\sqrt{\Sigma_e} \qquad (73)$$

Comparing the two amplitudes, we obtain

$$A = 1 - \frac{15\Sigma_e}{(11 + 6\nu - 5\nu^2)u_*^2} \tag{74}$$

from which a and $\tilde{a}_2$ follow again by Eqs. (44) and (54).

Hence, matching amplitudes in the hexagonal phase again leads to a linear relationship between A and Σ_e, but the prefactor differs compared with the plane-wave solution considered above.

However, irrespective of the chosen matching procedure, we obtain a linear relation between $\tilde{a}_2$ and $\tilde{c}$, leaving only one fitting parameter, $\tilde{c}$. Due to the linear dependence between $\tilde{a}_2$ and $\tilde{c}$ for both hexagonal and labyrinth patterns, one can use either matching relation to fit the experiments. Since the plane-wave (labyrinth) solution (67) leads to slightly simpler formulas, we choose the plane-wave matching in the following; that is, we assume that A and Σ_e are related by Eq. (69), and $\tilde{a}_2$ is given by Eq. (70). This convention means that we must determine $\tilde{c}$ by matching the theoretically predicted phase transition curve between the bistable and labyrinth states to the corresponding experimentally measured phase transition curve. The fitting value $\tilde{c}$ then automatically fixes the theoretical prediction for the second transition curve between hexagonal and bistable phase.

Phase diagram of the wrinkling morphology

The reduction of our effective theory to a standard Swift-Hohenberg equation allows us to make approximative predictions regarding the wrinkling morphologies. For the normal form, Eq. (65), three different wrinkling phases emerge depending on the choice of parameters A and B [14]:

Unwrinkled: $\qquad\qquad 1 - A \leq 0 \tag{75a}$

Hexagons: $\quad -\frac{1}{15}B^2 < 1 - A < \frac{4}{3}B^2 \tag{75b}$

Bistable phase: $\quad \frac{4}{3}B^2 < 1 - A < \frac{16}{3}B^2 \tag{75c}$

Labyrinths: $\qquad \frac{16}{3}B^2 < 1 - A \tag{75d}$

We recall that the coefficient B depends on κ via Γ_1, Γ_2, b and c, see Eq. (66), while A depends on the excess film stress and κ via Eq. (69). Substituting Eqs. (69) and (66) for A and B in Eq. (75), we obtain to leading order in κ the following stability criteria:

Unwrinkled: $\qquad\qquad \Sigma_e \leq 0 \tag{76a}$

Hexagons: $\quad -\frac{\rho}{20}\kappa^2 < \Sigma_e < \rho\kappa^2 \tag{76b}$

Bistable phase: $\qquad \rho\kappa^2 < \Sigma_e < 4\rho\kappa^2 \tag{76c}$

Labyrinths: $\qquad 4\rho\kappa^2 < \Sigma_e \tag{76d}$

where

$$\rho = \frac{1}{\left[\eta^{1/3}(1-\nu)\tilde{c}\right]^2} \tag{76e}$$

The free parameter $\tilde{c}$ is a function of $\eta = 3E_s/E_f$ and ν. The functional form of $\tilde{c} = \tilde{c}(\eta, \nu)$ determines how the phase transition lines depend on those material properties. Comparison with our experimental data suggests, however, that the phase transition lines are in fact independent of η and ν (Fig. 3 of Main Text). In this case, ρ must be independent of η and ν, which means that

$$\tilde{c} = \frac{c_1}{(1-\nu)\eta^{1/3}}, \tag{77}$$

with fit parameter c_1. Adopting the ansatz (77), we find that $c_1 = 0.0188 \pm 0.0002$ gives the best fit to the experimental data (Fig. 3 of Main Text). The resulting good agreement with the data suggests strongly that the critical curves, which separate the different wrinkling phases in our experiments, are independent of material properties.

Hysteresis

We explain how the critical curves in Fig. 4 of Main Text are obtained. To this end, recall that the amplitude of the hexagonal solutions is given by Eq. (72). Inserting Eq. (69) for A gives

$$\mathcal{A} = \frac{2}{15}\left[Bu_* + \sqrt{(Bu_*)^2 + \frac{45\Sigma_e}{4}}\right] \tag{78}$$

To compare with the labyrinth solutions, we consider the measurable difference U_H of the maximal and minimal values of the hexagonal displacement field u_H (measured in units of h). Equation (71) implies that

$$U_H = \max u_H - \min u_H = \frac{9}{2}\mathcal{A} \tag{79}$$

The prefactor in the last expression is due to the fact that u_H assumes its minimum at $-3\mathcal{A}$ and its maximum at $+3\mathcal{A}/2$.

To calculate the corresponding quantity U_L for the labyrinth solution u_L, we assume that labyrinths are locally described by the plane-wave $u_L = \mathcal{A}\cos(k_c x)$. We then obtain with Eqs. (68) and (69)

$$U_L = \max u_L - \min u_L = 2\sqrt{\Sigma_e} \tag{80}$$

Note that U_L is independent of curvature, whereas the square-root law for U_H is shifted horizontally and vertically by the Bu_*-terms (see Fig. 4b of Main Text). To first order in curvature, we have
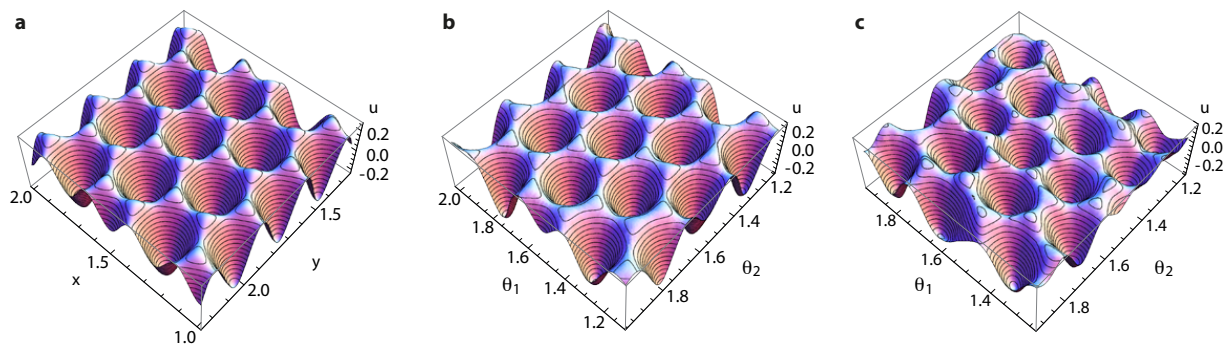
$$Bu_* \simeq \frac{3\kappa}{4c_1} \tag{81}$$

Fig. S1: Comparison of wrinkling morphologies in the hexagonal phase: (a) Planar analytical solution from Eq. (71), (b) numerical solution of the generalized Swift-Hohenberg theory from Eq. (43) (simulation parameters: $\gamma_0 = -0.08$, $a = 0.0151$, $c = 0.0095$, $R/h = 80$), and (c) 3D surface scan from experiments ($R = 20$mm, $h = 0.375$mm, $E_f = 2100$kPa, $E_s = 230$kPa). θ_1 and θ_2 denote polar angles.

yielding for the horizontal and vertical shifts (see Fig. 4b in the Main Text)

$$\delta\Sigma_e = \frac{\kappa^2}{20c_1^2}, \qquad \delta U_{\mathrm{H}} = \frac{9\kappa}{10c_1} \qquad (82)$$

Based on the results for U_{L} and U_{H}, we expect two hysteresis cycles (see Fig. 4 of Main Text). The first cycle is due to the shift $\delta\Sigma_e$, which creates a subcritical stability zone for the hexagonal solutions [14]. Increasing Σ_e from the unwrinkled phase, hexagons emerge at the onset $\Sigma_e = 0$. However, once they have formed, hexagons remain stable even if the excess stress Σ_e is subsequently reduced below the wrinkling onset $\Sigma_e = 0$. Only for $\Sigma_e < -\delta\Sigma_e$, hexagons loose stability and the unwrinkled solution remains as the only stable state. The second hysteresis cycle involves larger excess stresses (see Fig. 4a of Main Text). Starting from the hexagonal phase, hexagons remain stable if the excess stress is increased into the bistable phase [14]. Only if Σ_e is increased beyond the bistable-to-labyrinth transition line, hexagons loose their stability and the system jumps to a labyrinth state. Upon decreasing Σ_e from the labyrinth phase, the system adopts a different path as labyrinths remain stable throughout the bistable phase; a transition to hexagons happens when Σ_e is decreased below the critical value that separates the hexagonal from the bistable phase.

Validation of hexagonal patterns

To test our effective theory further, we compare the planar hexagon solution, Eq. (71), with the numerical solution of Eq. (43) on a spherical geometry (Fig. S1a,b). The good agreement between analytical and numerical solution confirms that the effective theory is indeed well approximated by the standard planar SH equation (65). These results corroborate that once hexagons are selected, curvature has negligible influence on their mor-

phology. Moreover, analytical and numerical solutions compare well with the experimentally determined 3D surface scans (Fig. S1c), demonstrating that the presented effective theory is able to reproduce the morphological details of thin film buckling patterns.

TOROIDAL GEOMETRIES

We consider a torus with major radius R_1 and minor radius R_2 measured in units of h. Using Eq. (1) and the standard surface parametrization $\mathbf{S} = [(R_1 + R_2\cos\theta_2)\cos\theta_1, (R_1 + R_2\cos\theta_2)\sin\theta_1, R_2\sin\theta_2]$ with coordinates $(\theta_1, \theta_2) \in [0, 2\pi] \times [0, 2\pi]$ we obtain the metric tensor

$$(a_{\alpha\beta}) = \begin{pmatrix} (R_1 + R_2\cos\theta_2)^2 & 0 \\ 0 & R_2^2 \end{pmatrix} \qquad (83)$$

Equation (5a) yields for the curvature tensor

$$(b_{\alpha\beta}) = \begin{pmatrix} -\cos\theta_2(R_1 + R_2\cos\theta_2) & 0 \\ 0 & -R_2 \end{pmatrix} \qquad (84)$$

and, from Eq. (26), one finds mean and Gaussian curvature as

$$\mathcal{H} = -\frac{1}{2}\left(\frac{\cos\theta_2}{R_1 + R_2\cos\theta_2} + \frac{1}{R_2}\right) \qquad (85a)$$

$$\mathcal{K} = \frac{\cos\theta_2}{R_1 R_2 + R_2^2\cos\theta_2} \qquad (85b)$$

Recall that the coefficients $\tilde{a}$, $\bar{\gamma}$, and $\tilde{a}_2$ were determined in the previous section using asymptotic comparison with the flat case. Hence, the expressions for these coefficients remain valid for toroidal geometries. Moreover, we observe that only the symmetry-breaking term in Eq. (34) contains contractions of the curvature tensor of first order, whereas the coefficients (33c) only depend on curvature at second or higher order. For instance, for

Fig. S 2: Wrinkling morphologies on a toroidal geometry with $R_1 = 80$ and $R_2 = 16$ for increasing excess film stress: (a) $\Sigma_e = 0.25$, (b) $\Sigma_e = 0.5$ and (c) $\Sigma_e = 2.0$. As in spherical geometries, one observes a transition from hexagonal to labyrinth-like patterns with increasing excess stress Σ_e. However, in contrast to the spherical case, the non-constant curvature on the torus can lead to local symmetry-breaking, i.e., at intermediate values of Σ_e labyrinth patterns are more likely to emerge at the inner saddle-like regions of the torus, see (b), whereas hexagons remain stable in the outer regions of the torus, where the two principal curvatures have the same sign resulting in a larger mean curvature. Simulation parameters are $\gamma_0 = -0.079$, $c = 0.075$, (a) $a = 0.017$, (b) $a = 0.016$, and (c) $a = 0.007$, using an unstructured surface triangulation with $> 26,000$ nodes.

a toroidal geometry with $R_1 = 80$, $R_2 = 16$, and $\eta = 0.33$ as shown in Fig. S2, we have $\gamma_0 = -0.079$, so that $|\gamma_0|$ is much larger than the maximum curvature correction $\max_{\theta_1, \theta_2} |\mathcal{R}/6| \approx 0.0007$. We can therefore neglect curvature corrections in the coefficients (33c).

Simulations of Eq. (34) confirm that a symmetry-breaking transition from hexagonal to labyrinth-like structures can also be observed on toroidal geometries when the excess stress is increased (Fig. S2). However, as curvature is now spatially varying, we find that the transition occurs first in the inner regions of the torus, where the principle curvatures have opposite sign (Fig. S2b). In the outside regions, where both principal components have the same sign, hexagons remain stable for relatively larger overstresses, until they become also unstable eventually (Fig. S2c).

In summary, Fig. S2 illustrates that the generalized theory derived above can be applied to arbitrarily curved surfaces.

[1] P. G. Ciarlet. *Mathematical elasticity, vol. III: Theory of shells.* North Holland, 2000.

[2] D. Breid and A. J. Crosby. Curvature-controlled wrinkle morphologies. *Soft Matter*, 9:3624–3630, 2013.

[3] M. M. Müller, M. Deserno, and J. Guven. Interface-mediated interactions between particles: A geometrical approach. *Phys. Rev. E*, 72(6):061407, 2005.

[4] W. Helfrich. Elastic properties of lipid bilayers: theory and possible experiments. *Z. Naturforsch.*, 28(11):693–703, 1973.

[5] Z. Y. Huang, W. Hong, and Z. Suo. Nonlinear analyses of wrinkles in a film bonded to a compliant substrate. *J. Mech. Phys. Solids*, 53:2101–2118, 2005.

[6] J. Swift and P. C. Hohenberg. Hydrodynamic fluctuations at the convective instability. *Phys. Rev. A*, 15(1):319–328, 1977.

[7] M. C. Cross and P. C. Hohenberg. Pattern formation outside of equilibrium. *Rev. Mod. Phys.*, 65(3):851–1112, 1993.

[8] H. G. Allen. *Analysis and Design of Structural Sandwich Panels.* Pergamon, New York, 1969.

[9] S. Cai, D. Breid, A. J. Crosby, Z. Suo, and J. W. Hutchinson. Periodic patterns and energy states of buckled films on compliant substrates. *J. Mech. Phys. Solids*, 59:1094–1114, 2011.

[10] L. D. Landau and E. M. Lifshitz. *Elasticity theory.* Pergamon Press, New York, 1975.

[11] Y. Jeong, Y.-C. Chen, M. K. Turksoy, S. Rana, G. Y. Tonga, B. Creran, A. Sanyal, A. J. Crosby, and V. M. Rotello. Tunable elastic modulus of nanoparticle monolayer films by host–guest chemistry. *Advanced Materials*, in press, doi: 10.1002/adma.201401226, 2014.

[12] G. Cao, X. Chen, C. Li, A. Ji, and Z. Cao. Self-assembled triangular and labyrinth buckling patterns of thin films on spherical substrates. *Phys. Rev. Lett.*, 100(3):036102, 2008.

[13] J. Yin, Z. Cao, C. Li, I. Sheinman, and X. Chen. Stress-driven buckling patterns in spheroidal core/shell structures. *Proc. Natl Acad. Sci.*, 105(49):19132–19135, 2008.

[14] A. A. Golovin and A. A. Nepomnyashchy. *Self-assembly, pattern formation and growth phenomena in nano-systems.* Springer, Dordrecht, 2006.